Arabian Journal of Chemistry (2022) **15**, 103804

King Saud University

**Arabian Journal of Chemistry**

www.ksu.edu.sa
www.sciencedirect.com

ORIGINAL ARTICLE

# Influence of the particle size on the antibacterial activity of green synthesized zinc oxide nanoparticles using *Dysphania ambrosioides* extract, supported by molecular docking analysis

**Rafael Álvarez-Chimal [a,b], Víctor I. García-Pérez [c], Marco Antonio Álvarez-Pérez [d], Rosario Tavera-Hernández [e,f], Lorena Reyes-Carmona [b,c], Miryam Martínez-Hernández [c], Jesús Ángel Arenas-Alatorre [a,*]**

[a] *Laboratorio 113 Síntesis de Nanomateriales Magnéticos, Departamento de Materia Condensada, Instituto de Física, Universidad Nacional Autónoma de México, Ciudad Universitaria, Ciudad de México, Coyoacán, 04510, Mexico*
[b] *Programa de Maestría y Doctorado en Ciencias Médicas, Odontológicas y de la Salud, Universidad Nacional Autónoma de México, Ciudad Universitaria, Ciudad de México, Coyoacán, 04510, Mexico*
[c] *Laboratorio de Biointerfases, División de Estudios de Posgrado e Investigación, Facultad de Odontología, Universidad Nacional Autónoma de México, Ciudad Universitaria, Ciudad de México, Coyoacán, 04510, Mexico*
[d] *Laboratorio de Bioingeniería de Tejidos, División de Estudios de Posgrado e Investigación, Facultad de Odontología, Universidad Nacional Autónoma de México, Ciudad Universitaria, Ciudad de México, Coyoacán, 04510, Mexico*
[e] *Laboratorio 2-10, Departamento de Productos Naturales, Instituto de Química, Universidad Nacional Autónoma de México, Ciudad Universitaria, Ciudad de México, Coyoacán, 04510, Mexico*
[f] *Programa de Maestría y Doctorado en Ciencias Químicas, Universidad Nacional Autónoma de México, Ciudad Universitaria, Ciudad de México, Coyoacán, 04510, Mexico*

Received 16 December 2021; accepted 15 February 2022
Available online 21 February 2022

**KEYWORDS**

Antibacterial;
ZnO nanoparticles;
Green synthesis;
Molecular docking;

**Abstract** Bacteria-associated infections have increased in recent years due to treatment resistance developed by these microorganisms. Due to the high antibacterial capacity associated with their nanometric size, nanoparticles, such as zinc oxide (ZnO), have proven to be an alternative for general medical procedures. One of the methodologies to synthesize them is green synthesis, where the most commonly used resources are plant species. Using *Dysphania ambrosioides* extract at various

* Corresponding author at: Laboratorio 113 Síntesis de Nanomateriales Magnéticos, Departamento de Materia Condensada, Instituto de Física, Universidad Nacional Autónoma de México, México, Ciudad de México, Ciudad Universitaria, Coyoacán 04510, Mexico.
E-mail address: jarenas@fisica.unam.mx (J.Ángel Arenas-Alatorre).
Peer review under responsibility of King Saud University.

Production and hosting by Elsevier

https://doi.org/10.1016/j.arabjc.2022.103804

Characterization;
Heat treatment

synthesis temperatures (200, 400, 600, and 800 °C), zinc oxide nanoparticles (ZnO-NPs) with average sizes ranging from 7 to 130 nm, quasi-spherical shapes, and hexagonal prism shapes were synthesized. Larger sizes were obtained by increasing the synthesis temperature. The ZnO crystalline phase was confirmed by X-ray diffraction and transmission electron microscopy. The sizes and shapes were observed by field emission scanning electron microscopy. The Zn-O bond vibration was identified by Fourier transform infrared spectroscopy. Thermogravimetry showed the stability of ZnO-NPs. The antibacterial evaluations, disk diffusion test, and minimum bactericidal concentration, demonstrated the influence of particle size. The smaller the nanoparticle size, the higher the inhibition for all pathogenic strains: *Staphylococcus aureus*, *Staphylococcus epidermidis*, *Escherichia coli*, *Pseudomonas aeruginosa*, and dental pathogens: *Streptococcus mutans*, *Streptococcus sanguinis*, *Porphyromonas gingivalis,* and *Prevotella intermedia*. The molecular docking study showed a favorable interaction between ZnO-NPs and some proteins in Gram-positive and Gram-negative bacteria, such as TagF in *Staphylococcus epidermidis* and AcrAB-TolC in *Escherichia coli*, which led to proposing them as possible targets of nanoparticles.



## 1. Introduction

In recent years, the number of infections associated with antibiotic-resistant bacteria has increased. Bacteria are capable of developing resistance mechanisms. Antibiotic resistance can be acquired through multiple pathways that include alteration or inactivation of the antibiotic, modification of the target, or a metabolic pathway to avoid its harmful effects, to mention a few (Webster and Seil, 2012).

A compelling alternative is provided by nanoparticles (NPs), which rely on entirely different mechanisms of antibacterial activity than antibiotics. For all varieties of NPs, the antibacterial mechanism is not fully understood. The specific surface area of NPs increases as the particle size decreases, allowing the material to interact more closely with the environment. The chemistry, size, and shape of the NPs are some of the characteristics that influence their antibacterial properties (Ahmed et al., 2021; Carrouel et al., 2020; Webster and Seil, 2012).

The antibacterial properties of NPs are based on the fact that, due to their nanometric size, they have a higher surface area to volume ratio, which provides them with more vital interaction with microbial structures and thus exerts their antibacterial activity, besides leading to reactive oxygen species (ROS) generation and ions release that affects bacteria proteins and deoxyribonucleic acid (DNA), apart from the fact that bacteria have not developed very efficient resistance mechanisms against NPs (Carrouel et al., 2020; Sirelkhatim et al., 2015).

Green synthesis is one of the methodologies that have relevance in NPs synthesis, whose purpose is to design chemical processes that reduce or eliminate hazardous substances (Anastas and Warner, 2014).

This methodology allows synthesizing NPs of different sizes and shapes, carrying out this procedure without the use of special equipment such as lasers or reactors (Abdelghany et al., 2019; Ahmed et al., 2020a, 2020b; Mostafa and Menazea, 2020), several substances or reagents that may be dangerous or expensive (Salavati-Niasari, 2004, Salavati-Niasari, et al., 2009), surfactants (Ghanbari et al., 2013; Salavati-Niasari et al., 2008, 2010a), catalysts (Salavati-Niasari et al., 2004), in addition to reducing synthesis times (Mortazavi-Derazkola et al., 2015; Salavati-Niasari et al., 2010b) by involving fewer steps and even taking advantage of organic waste material (Menazea et al., 2021).

One of the most commonly used resources to perform green synthesis is vegetal species. Several plant metabolites, including terpenes, polyphenols, carbohydrates, alkaloids, and proteins, play an essential role in NPs synthesis (Salinas Estevané and Sánchez Cervantes, 2012). In particular, the source of the plant extract influences the synthesized sizes and shapes. Different concentrations of metabolites in plant extracts lead to differences in the synthesized NPs depending on other factors such as metal ion concentration, pH, time, and temperature (Agarwal et al., 2017; Makarov et al., 2014).

Previously, *Dysphania ambrosioides* extract was used for silver NPs (Ag-NPs) (Carrillo-López et al., 2014; Carrillo-López et al., 2016) and zinc oxide NPs (ZnO-NPs) (Álvarez-Chimal et al., 2021) green synthesis with different particle sizes. However, the synthesized ZnO-NPs were from 5 to 30 nm, quasi-spherical in shape, and ZnO crystalline phase. Moreover, ZnO-NPs inhibited the growth of *Staphylococcus aureus*, *Staphylococcus epidermidis*, *Escherichia coli*, *Streptococcus mutans*, *Streptococcus sanguinis*, *Porphyromonas gingivalis*, *Prevotella intermedia,* and *Aggregatibacter actinomycetemcomitans* bacterial strains (Álvarez-Chimal et al., 2021).

Aside from their antibacterial activity (Abebe et al., 2020; Kumar et al., 2017; Mishra et al., 2017;), ZnO-NPs are chemically inert, water-insoluble, and have high mechanical strength and low toxicity (Özgür et al., 2005). Therefore, ZnO is useful as a matrix to transport and stabilize drugs (Vasile et al., 2014). It has therapeutic properties for irritations and superficial wounds due to its astringent and antibacterial properties (Agarwal et al., 2017), which make it of medical and dental interest.

The molecular docking approach can be used to model the interaction between a small molecule, such as NPs, and proteins at the atomic level, which allows to characterize the behavior of this small molecule in the binding site of target proteins as well as to elucidate biochemical processes such as the antibacterial mechanism of NPs (Ismail et al., 2021; McConkey et al., 2002; Meng et al., 2011).

This work presents a green and fast methodology for the ZnO-NPs synthesis of different particle sizes without adding any surfactant or catalyst and without using special equipment. The antibacterial properties of the synthesized ZnO-NPs against pathogenic strains of medical and dental interest were studied in depth. Furthermore, this is one of the first studies to use molecular docking analysis to evaluate the binding modes of ZnO-NPs with bacterial proteins, providing a better understanding of the antibacterial mechanism.

Taking into account the above, this research aimed to deepen the antibacterial properties of ZnO-NPs of different particle sizes green synthesized using *Dysphania ambrosioides* extract on pathogenic strains such as *Staphylococcus aureus*, *Staphylococcus epidermidis*, *Escherichia coli*, *Pseudomonas aeruginosa*, and dental pathogens such as *Streptococcus mutans*, *Streptococcus sanguinis*, *Porphyromonas gingivalis*, and *Prevotella intermedia*. The resulting NPs were characterized by X-ray diffraction, field emission scanning electron microscopy, transmission electron microscopy, high-resolution electron microscopy, X-ray energy dispersive spectroscopy, Fourier transform infrared spectroscopy, and thermogravimetry. The antibacterial evaluations were by disk diffusion test and determination of the minimum bactericidal concentration. Finally, to contribute to the understanding of the antibacterial mechanism of green synthesized ZnO-NPs, a molecular docking study was performed to determine the pos-

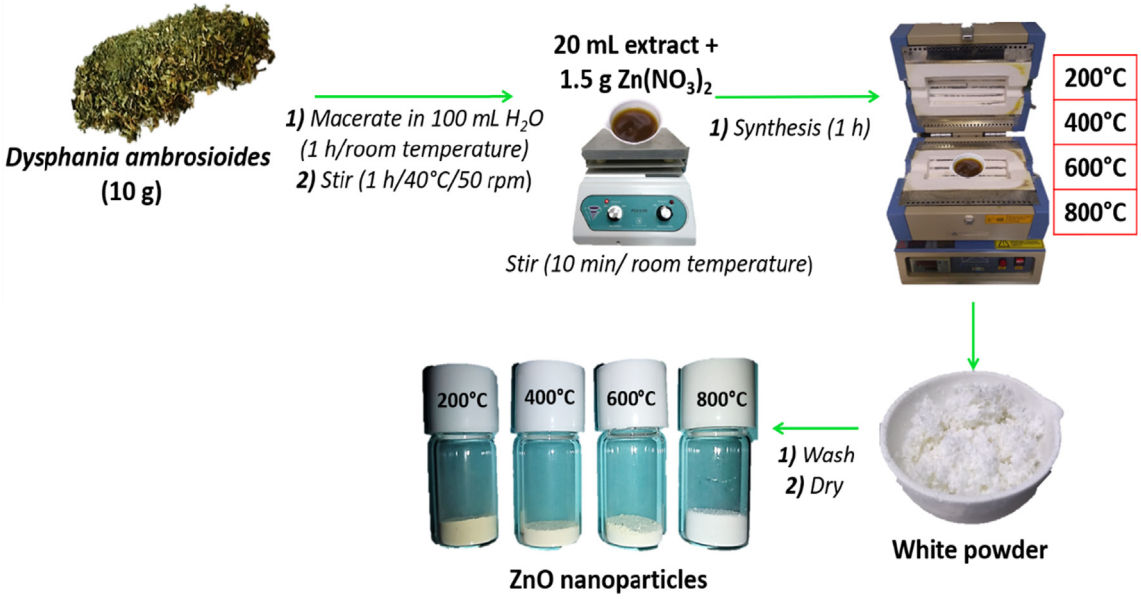


**Fig. 1** Green synthesis of ZnO-NPs of different particle sizes.

sible interaction of ZnO-NPs with some proteins in Gram-positive and Gram-negative bacteria, such as TagF in *Staphylococcus epidermidis* and AcrAB-TolC in *Escherichia coli*.

## 2. Materials and methods

### 2.1. Materials

Dried leaves of *Dysphania ambrosioides* and 99.0% purity zinc nitrate hexahydrate ($Zn(NO_3)_2{\cdot}6H_2O$) purchased from Meyer were used to perform the green synthesis of the ZnO-NPs. 300-mesh carbon-coated copper grids for TEM. For the antibacterial tests, trypticase soy agar (TSA) and trypticase soy broth (TSB) purchased from BD Bioxon, defibrinated sheep blood, and deionized water were used.

### 2.2. Green synthesis of ZnO-NPs

10 g of *Dysphania ambrosioides* dried leaves were macerated in 100 mL of deionized water for 1 h at room temperature without stirring. Then, the mixture was stirred for 2 h at 40 °C and 50 rpm. The synthesis was performed by mixing 20 mL of previously obtained extract (pH = 6.8) with 1.5 g of $Zn(NO_3)_2{\cdot}6H_2O$ and stirring for 10 min at room temperature (pH = 3.6) before being placed in a muffle for 1 h at the reaction temperature (200, 400, 600, and 800 °C). It was then removed from the muffle and allowed to cool at room temperature. The resulting powders from each synthesis were washed in triplicate with deionized water and allowed to dry at room temperature for 24 h (Álvarez-Chimal et al., 2021; Geetha et al., 2016) (Fig. 1).

### 2.3. Characterization

The resulting powders from the synthesis at different temperatures were characterized by X-ray diffraction (XRD), field emission scanning electron microscopy (FESEM), transmission electron microscopy (TEM), and high-resolution electron microscopy (HRTEM), X-ray energy dispersive spectroscopy (EDS), Fourier transform infrared spectroscopy (FTIR) and thermogravimetry (TG).

XRD was used to examine the crystalline structure using a Bruker AXS D8 Advance X-ray diffractometer at a voltage of 40 kV and a current of 30 mA with Cu K radiation (1.541) between 2θ angles of 4° and 110°. The XRD results were indexed using the powder diffraction file (PDF) #891397 for the ZnO.

The average crystalline size was calculated by the Debye-Scherrer equation.

$$D = K\,\lambda/B\cos\theta$$

Where: D: average crystalline size; K: shape factor usually taken as 0.9; λ: wavelength of the X-ray radiation (k = 1.54 1 Å) for $\lambda_{K\alpha}$Cu; θ: Bragg diffraction angle; B: line width at a half-maximum height.

For FESEM analysis, the samples were mounted on an aluminum sample holder with conductive carbon tape. A JEOL field emission electron microscope, model JSM7800F, with a resolution of 0.7 nm was used, equipped with an OXFORD microprobe for EDS analysis.

For TEM analysis, the samples were placed on the 300-mesh carbon-coated copper grids. A JEOL transmission electron microscope model JEM 2010 FEG was used, with a resolution of 0.19 nm, equipped with a NORAN microprobe Voyager model for EDS analysis. Measurements of the interplanar distances were recorded in HRTEM images using the Fast Fourier Transform (FFT) in Digital Micrograph software from GATAN.

In FTIR analysis, a Bruker Tensor 27 FTIR spectrophotometer was used in the 4000–500 $cm^{-1}$ wavelength region. The analysis was performed by placing the samples in a KBr pellet.

For TG analysis, a TA Instruments model SDT Q600 thermo analyzer was used, under air atmosphere conditions, from 10 to 800 °C with a 10 °C/min increase.

**Table 1** Bacterial strains tested.

| | Gram-positive | Gram-negative |
|---|---|---|
| **Aerobic** | *Staphylococcus aureus* (ATCC 25923) | *Escherichia coli* (ATCC 33780) |
| | *Staphylococcus epidermidis* (ATCC 14990) | *Pseudomonas aeruginosa* (ATCC 43536) |
| **Anaerobic** | *Streptococcus mutans* (ATCC 25275) | *Porphyromonas gingivalis* (ATCC 33277) |
| | *Streptococcus sanguinis* (ATCC 10556) | *Prevotella intermedia* (ATCC 25611) |

### 2.4. Antibacterial test

#### 2.4.1. Disk diffusion test

The disk diffusion test (Kirby-Bauer method) (Gunalan et al., 2012; Meraat et al., 2016) was used to evaluate the synthesized ZnO-NPs at 81400 μg/mL (1 M) and 40700 μg/mL (0.5 M) concentrations on different bacterial strains of medical and dental interest (Table 1).

Under sterile conditions, ZnO-NPs suspensions at the concentrations to be evaluated were prepared and kept under stirring. First, each bacterial culture was adjusted to an optical density of 1 (OD = 1) and grown in TSA for aerobic bacteria and TSA with 5% defibrinated sheep blood for anaerobic bacteria. Then, 6 mm diameter filter paper disks were placed on the already sown culture media. Next, 5 μL of ZnO-NPs suspension were distributed on the filter paper disk in duplicate. Chlorhexidine (2100 μg/mL) was used as a positive control and sterile TSB as a negative control (0 μg/mL). Aerobic bacteria were incubated at 35 °C for 18 to 24 h and anaerobic bacteria for 48 to 72 h at the same temperature and under anaerobic conditions. After the incubation times, the inhibition diameters generated were measured.

#### 2.4.2. Minimum bactericidal concentration (MBC)

The determination of MBC was performed by the microdilution method in broth culture in 96-well plates (Meraat et al., 2016). ZnO-NPs suspensions were prepared at concentrations ranging from 81400 μg/mL (1 M) to 5088 μg/mL (0.063 M). 100 μL of each suspension were placed in the wells in duplicate. Each well with ZnO-NPs was aseptically inoculated with 10 μL of a bacterial suspension at a concentration of $10^7$ bacteria/mL. Chlorhexidine (2100 μg/mL) was used as a positive control and sterile TSB as a negative control. Plates were incubated, shaking at 180 rpm for 24 h at 35 °C for aerobic bacteria and 72 h for anaerobic bacteria at the same temperature and under anaerobic conditions. After the incubation times, the contents of the wells were transferred to plates with TSA or TSA with 5% defibrinated sheep blood, depending on the type of bacteria, and incubated under the same conditions specified above. The MBC is defined as the lowest concentration of ZnO-NPs able to eliminate 99.9% of the bacterial inoculum at the end of the incubation time (no bacterial growth is observed).

Statistical analysis was done by two-way ANOVA with Tukey's post hoc test. Statistical differences are considered with $p \leq 0.05$.

### 2.5. Molecular docking

Binding mode estimation between ZnO-NPs and the bacterial proteins TagF enzyme, involved in teichoic acid polymer synthesis in *Staphylococcus epidermidis* (Lovering et al., 2010) and AcrAB-TolC protein, an efflux pump that vectorially transports compounds with low chemical similarity in *Escherichia coli* (Du, et al., 2014), was performed by molecular docking.

ZnO-NPs were generated in Avogadro software by assigning a 5 × 5 × 5 Å surface area, Marsilli-Gasteiger charges were added to the ZnO-NPs in MGL Tools 1.5.6 software. The crystallized structures of the proteins were taken from the protein database (PDB), TagF polymerase (PDB ID: 3L7I), and the AcrAB-TolC pump (PDB ID: 5NG5). The A chain from the TagF enzyme was selected for the analysis. Solvent residues were removed in UCSF Chimera 1.15 software, polar hydrogens and Kollman charges were added in MGL Tools 1.5.6, grid size was 60 × 60 × 60 Å with 0.375 Å spacing and center at x: −146.318, y: 85.698, and z: 13.278 covering all amino acids from the enzyme catalytic site, AutoDock 4.2 default parameters were assigned, and Lamarckian genetic algorithms were selected. A, B, D, E, G, and H chains from the AcrAB-TolC pump were considered for the analysis; solvent residues were removed in UCSF Chimera 1.15 software, polar hydrogens and Kollman charges were added in MGL Tools 1.5.6, the grid size was 120 × 104 × 88 Å with 0.375 Å spacing and center at x: 200.504, y: 200.518, and z: 198.92, AutoDock 4.2 default parameters were assigned and Lamarckian genetic algorithms were selected. Finally, the images were generated using Pymol software in both cases.

## 3. Results

### 3.1. Green synthesis of ZnO-NPs

The powders produced by the green synthesis of ZnO-NPs at 200 °C (ZnO-NPs 200 °C), 400 °C (ZnO-NPs 400 °C), 600 °C (ZnO-NPs 600 °C), and 800 °C (ZnO-NPs 800 °C) were of various shades of white (Fig. 2a).

### 3.2. X-ray diffraction

The diffraction patterns from all synthesized ZnO-NPs (Fig. 2b) showed the Bragg reflections indicated to ZnO (PDF #891397), 2θ values were 31.74°, 34.38°, 36.21°, 47.49°, 56.54°, 62.78°, 66.30°, 67.87°, 69.00°, 72.47°, 76.87°, 81.28°, and 89.50°, the reflections were indexed as (100), (002), (101), (102), (110), (103), (200), (112), (201), (004), (202), (104), and (203) respectively. The ZnO crystalline structure is hexagonal with lattice parameters of $a = b = 3.252$ Å and $c = 5.213$ Å.

The average crystalline size calculated by the Debye-Scherrer equation (Table 2) showed that the average crystalline size increased as the synthesis temperature was higher.

### 3.3. X-ray energy dispersive spectroscopy

The EDS analysis of the synthesized ZnO-NPs showed the atomic percentages of Zn and O in all syntheses was close to 50% (Table 3). A 1:1 ratio of both elements was established,

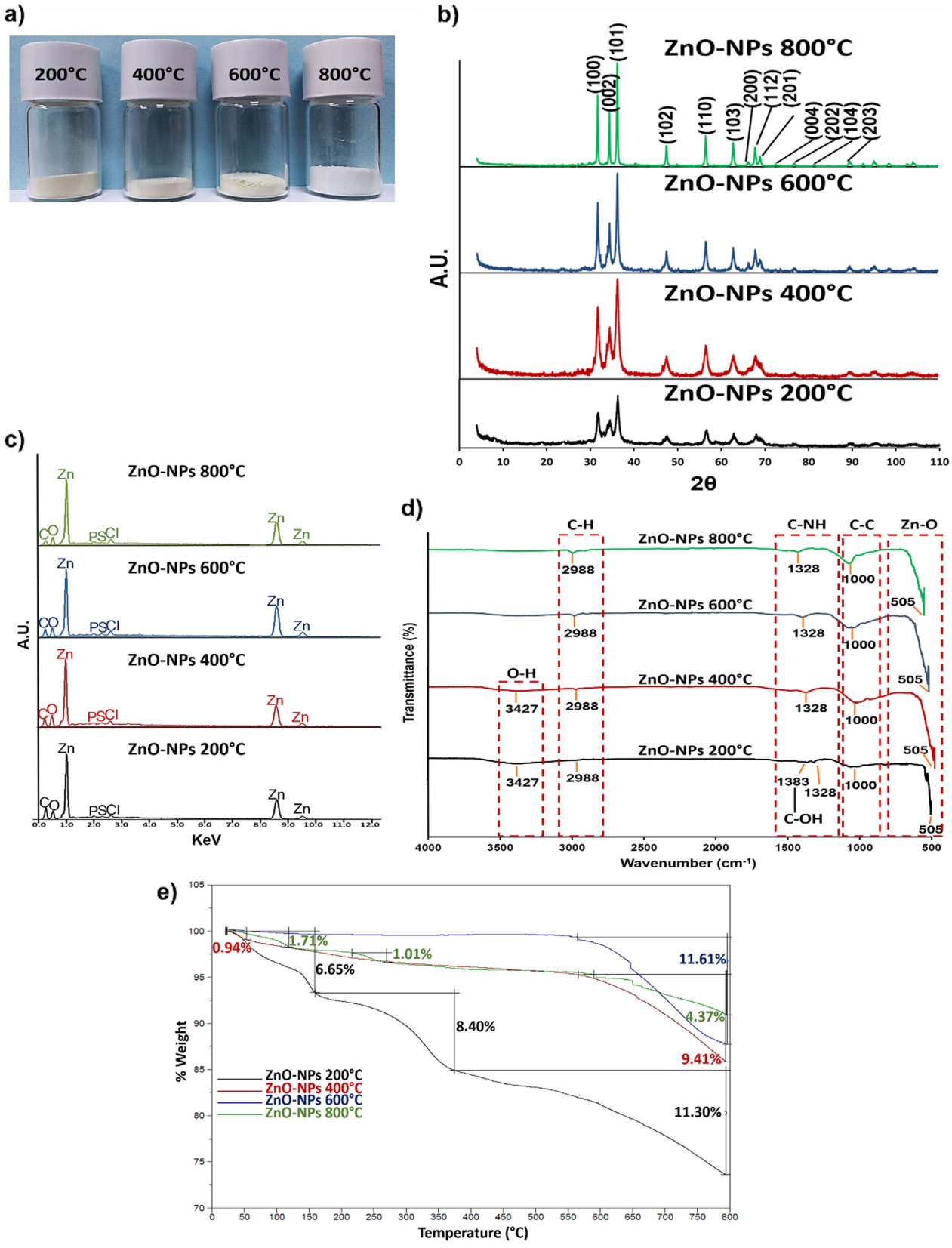


**Fig. 2** a) Resulting powders from the different synthesis temperatures (200, 400, 600, and 800 °C). b) XRD diffraction patterns of synthesized ZnO-NPs. Crystalline planes (Miller indexes) corresponding to ZnO were observed in all syntheses. c) The EDS spectra of the synthesized ZnO-NPs at different temperatures. In addition to other elements, Zn and O signals were detected. d) The FTIR spectra of the synthesized ZnO-NPs. e) The TG analysis of the synthesized ZnO-NPs at different temperatures.

supporting the confirmation of ZnO synthesis at different temperatures. Other elements besides Zn and O (Fig. 2c), such as C (0.09%), P (0.04%), S (0.02%), and Cl (0.02%), came from the vegetal species used, but their atomic percentages do not modify the 1:1 ratio of Zn and O.

### 3.4. Fourier transform infrared spectroscopy

The FTIR spectra of synthesized ZnO-NPs at different temperatures show (Fig. 2d) that 505 $cm^{-1}$ vibration belongs to the Zn-O bond stretching mode. The other vibrations belong to the functional groups of the organic compounds that participated in the synthesis. The 1000 $cm^{-1}$ vibration is due to the C-C bond. 1383 $cm^{-1}$ and 1328 $cm^{-1}$ vibrations are attributed to the C-OH and C-NH bonds, respectively. The C-H bond vibrates at 2988 $cm^{-1}$, and the O-H bond vibrates at 3427 $cm^{-1}$, which appears only in ZnO-NPs 200 °C and ZnO-NPs 400 °C (Anvekar et al., 2017; Khan et al., 2015; Liu et al., 2019; Santhoshkumar et al., 2017; Umar et al., 2018).

### 3.5. Thermogravimetry

The TG analysis (Fig. 2e) showed that ZnO-NPs 200 °C had three weight losses, one of 6.65% at 100 °C, the other of 8.40% at 150 °C, and finally a weight loss of 11.30% at around 400 °C. After the process, 25% of the initial weight of these NPs was lost. The ZnO-NPs 400 °C were more stable. A loss of 0.94% at 100 °C, then they remained stable until 550 °C, where there was a loss of 9.41% of their weight. At the end of the process, only near 10% of the initial weight was lost. The ZnO-NPs 600 °C were the most stable until about 550 °C, which they lost 11.61% of the initial weight. The ZnO-NPs 800 °C had similar behavior to ZnO-NPs 400 °C. A loss of 1.71% at 100 °C, 1.01% at around 250 °C, and 9.41% at 550 °C. At the end of the treatment, there was a weight loss of approximately 12%. The reasons for each weight loss are explained in the discussion section.

**Table 2** Average crystalline sizes (±standard deviation).

| ZnO-NPs | Average crystalline size (nm) |
|---|---|
| ZnO-NPs 200 °C | 6.74 (±3.17) |
| ZnO-NPs 400 °C | 10.10 (±2.68) |
| ZnO-NPs 600 °C | 16.37 (±3.53) |
| ZnO-NPs 800 °C | 29.53 (±5.90) |

**Table 3** Atomic percentages (% at) of Zn and O in synthesized ZnO-NPs.

| ZnO-NPs | Zn (% at) | O (% at) |
|---|---|---|
| ZnO-NPs 200 °C | 49.58 | 50.42 |
| ZnO-NPs 400 °C | 50.76 | 49.24 |
| ZnO-NPs 600 °C | 52.68 | 47.32 |
| ZnO-NPs 800 °C | 53.40 | 46.60 |

### 3.6. Field emission scanning electron microscopy

The FESEM images (Fig. 3) showed that the ZnO-NPs 200 °C were quasi-spherical in shape (Fig. 3a). Their particle sizes ranged from 4 to 10 nm, with an average of 7 nm. The ZnO-NPs 400 °C were also quasi-spherical in shape (Fig. 3b). The particle size ranged from 8 to 24 nm, with an average of 14 nm. The ZnO-NPs 600 °C (Fig. 3c) had two shapes: quasi-spherical and hexagonal prisms. The quasi-spherical shaped particle sizes ranged from 12 to 45 nm with an average of 22 nm, while the hexagonal prisms ranged from 20 to 100 nm with an average of 70 nm. Finally, the ZnO-NPs 800 °C (Fig. 3d) also exhibited two shapes, quasi-spherical and hexagonal prisms. The quasi-spherical shaped particle sizes ranged from 50 to 200 nm with an average of 130 nm, and hexagonal prisms ranged from 30 to 140 nm with an average of 90 nm. It was observed that, as the synthesis temperature increased, the size of the NPs was larger, and at 600 and 800 °C, a new shape appeared.

### 3.7. Transmission electron microscopy

The TEM images (Fig. 4 and Fig. 5) showed the crystallinity of the synthesized ZnO-NPs. The crystalline planes and interplanar distances belonged to ZnO using PDF #891397 for ZnO as a reference. The quasi-spherical-shaped ZnO-NPs 200 °C were observed (Fig. 4a). High-resolution transmission electron microscopy (HRTEM) image analysis of an irregularly shaped nanoparticle (Fig. 4b) confirmed the presence of ZnO crystalline planes by fast Fourier transform (FFT) in the [0 1 0] direction. The HRTEM analysis of the quasi-spherical shaped NPs-ZnO 400 °C of larger size (Fig. 4c) confirmed the presence of ZnO crystalline planes (Fig. 4d). The NPs-ZnO 600 °C showed the quasi-spherical and elongated shapes with hexagonal faces along the "C" growth axis of the hexagonal prisms (Fig. 5a). The FFT analysis of both shapes (Fig. 5b and 5e) demonstrated the presence of ZnO crystalline planes. The same analysis was performed for quasi-spherical and hexagonal prism shapes of the NPs-ZnO 800 °C (Fig. 5c). FFT analysis (Fig. 5d and 5f) of both shapes confirmed the presence of ZnO crystalline planes. These analyses supported the confirmation of ZnO synthesis, and the hexagonal crystalline structure of this compound could be appreciated, confirming the XRD analysis.

### 3.8. Disk diffusion test

Once ZnO-NPs of different particle sizes were synthesized, antibacterial tests were performed to determine the influence of particle size on this biological activity.

This test showed inhibition of all the bacterial strains evaluated, both Gram-positive and Gram-negative, with both concentrations of ZnO-NPs (Fig. 6a). It was observed that the inhibition diameters generated were more significant as the size of the NPs decreased, as well as that at a high concentration, the inhibition increased. *Pseudomonas aeruginosa* was the most resistant to ZnO-NPs, inhibited at the highest concentration with the smallest ZnO-NPs (4–10 nm); *Streptococcus sanguinis* and *Prevotella intermedia* were the most sensitive, with larger inhibition diameters at both ZnO-NPs concentrations, even greater than those generated by chlorhexidine. Inhibition

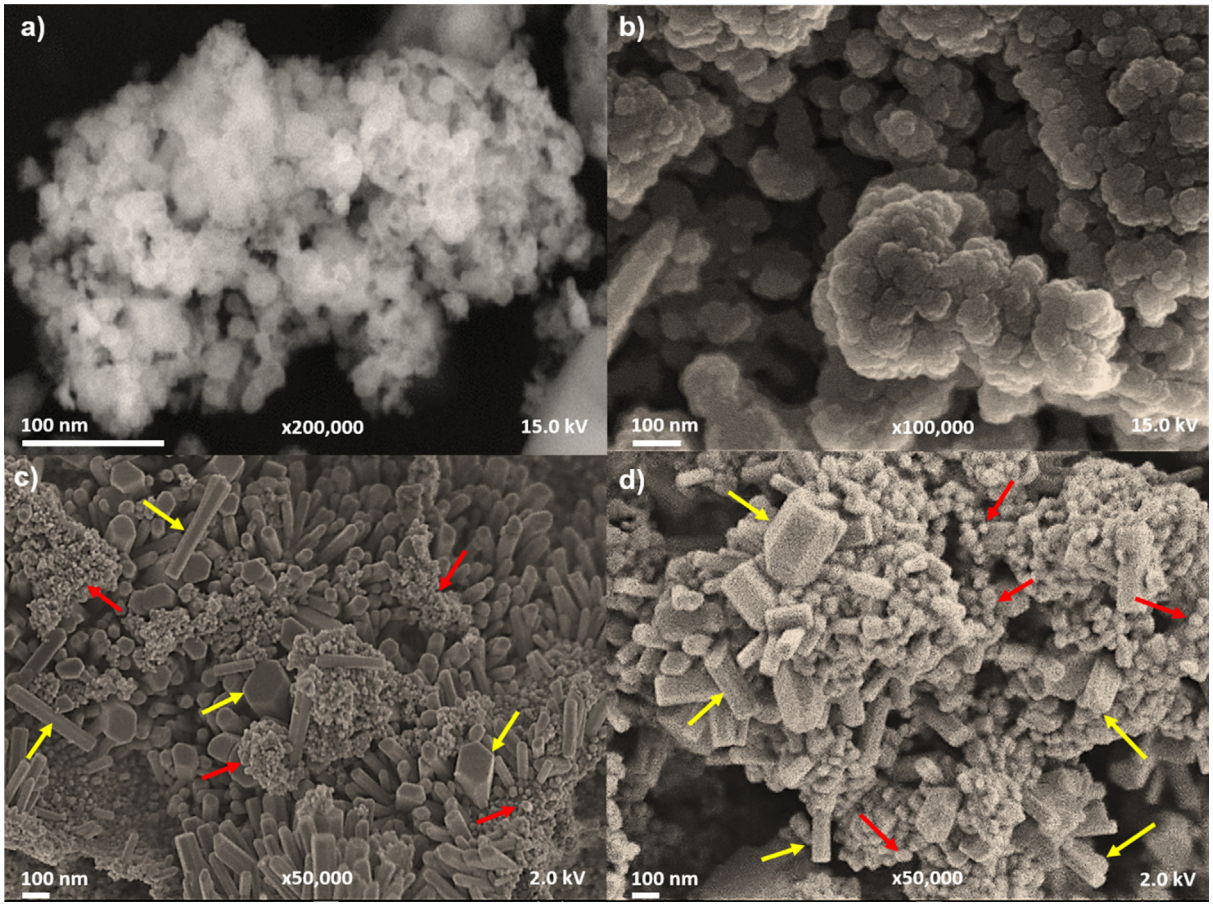


**Fig. 3** FESEM images of synthesized ZnO-NPs. a) Quasi-spherical shapes of ZnO-NPs 200 °C. b) Quasi-spherical shape of ZnO-NPs 400 °C. c) Quasi-spherical (red arrows) and hexagonal prism (yellow arrows) shapes of ZnO-NPs 600 °C. d) The hexagonal prism shapes (yellow arrows) and quasi-spherical shapes (red arrows) of ZnO-NPs 800 °C.

diameters caused by ZnO-NPs were generally smaller than those produced by chlorhexidine used as a positive control.

### *3.9. Minimum bactericidal concentration*

By MBC determination, the influence of particle size over the elimination of bacterial strains was observed (Fig. 6b); a smaller particle size led to a lower MBC; observed in *Staphylococcus aureus* and *Escherichia coli* strains. *Staphylococcus epidermidis*, *Porphyromonas gingivalis,* and *Prevotella intermedia* were the most sensitive to ZnO-NPs. There was no influence on particle size; all ZnO-NPs eliminated these strains at the lowest concentration evaluated. *Streptococcus sanguinis* was also sensitive to ZnO-NPs, and no influence of particle size was observed with the smallest ZnO-NPs. With the larger ones (50–200 nm), the MBC increased. *Streptococcus mutans* was sensitive to ZnO-NPs. The influence of particle size was also observed. The smallest ZnO-NPs (4–10 nm and 8–24 nm) led to a lower MBC, while with larger ZnO-NPs the MBC was increased. *Pseudomonas aeruginosa* was the most resistant to ZnO-NPs, the MBC was the highest. Only the smallest ZnO-NPs (4–10 nm) were able to eliminate it at low MBC. In all cases, the MBCs achieved by ZnO-NPs were higher than those of chlorhexidine and agreed with disk diffusion test results.

### *3.10. Molecular docking*

According to antibacterial test results, *Staphylococcus epidermidis* and *Escherichia coli* strains were sensitive to ZnO-NPs, so molecular docking was performed to analyze the possible binding mode of ZnO-NPs to TagF polymerase in *Staphylococcus epidermidis* and the AcrAB-TolC pump in *Escherichia coli*, which were considered as potential antibacterial targets. The free binding energy of −7.54 Kcal/mol and the inhibition constant of 2.99 μM were calculated for the TagF polymerase. The ZnO-NPs formed hydrogen bonds with arginine 548 and histidine 584 amino acids (Fig. 7a). Histidine 584 is part of the catalytic domain of this enzyme (Lovering et al., 2010). The free binding energy of −7.36 Kcal/mol and the inhibition constant of 4.02 μM were calculated for the AcrAB-TolC pump. The ZnO-NPs formed hydrogen bonds with glutamine 71 and threonine 177 amino acids of the AcrA portion, involved in the interaction with the periplasmic space (Du et al., 2014) of these bacteria (Fig. 7b).

## 4. Discussion

ZnO is a versatile, inorganic, polar, non-toxic, crystalline, chemically stable, and safe mineral found in the earth's crust

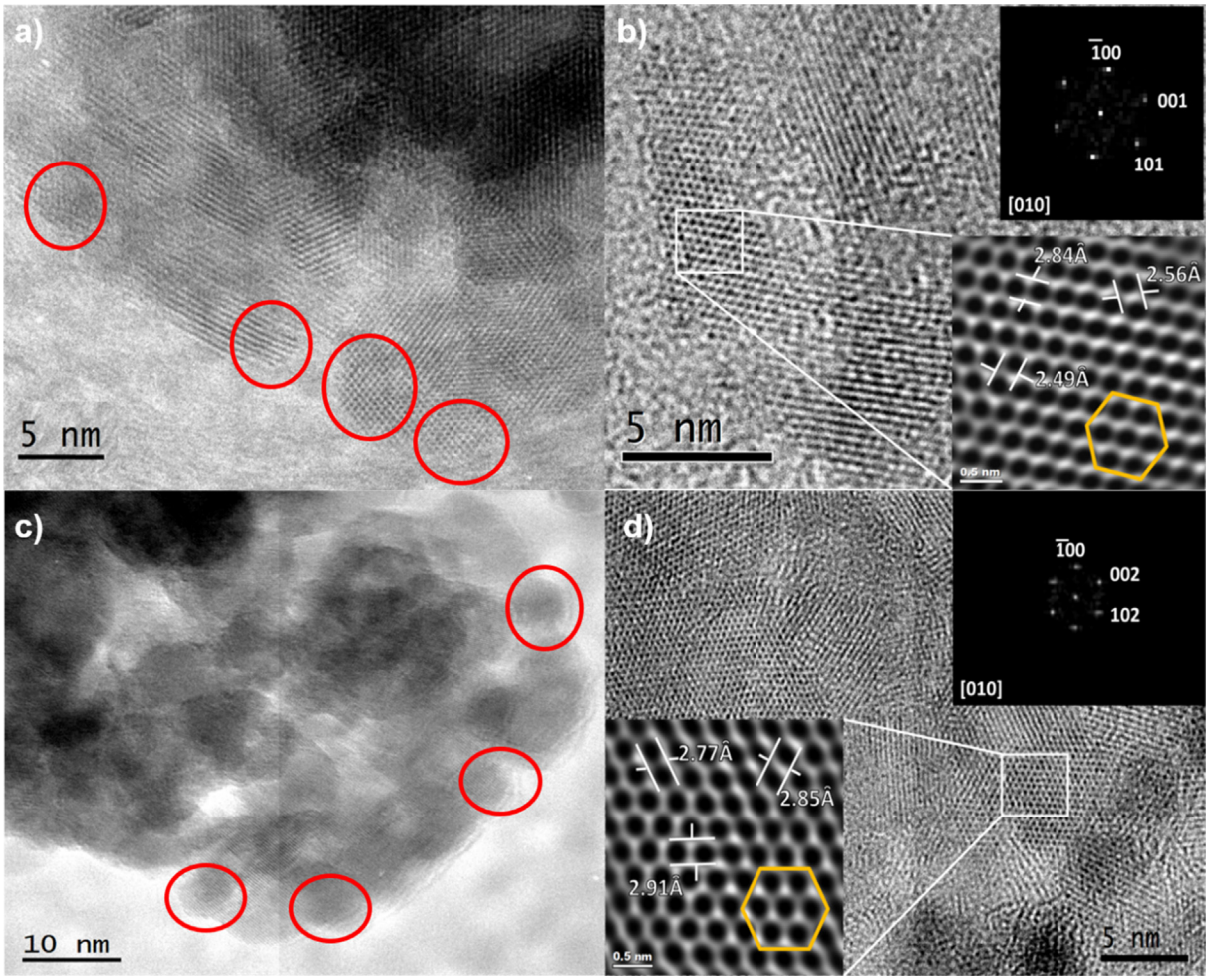


**Fig. 4** TEM images of ZnO-NPs 200 °C and ZnO-NPs 400 °C. a) ZnO-NPs 200 °C with quasi-spherical shapes (red circles). b) The HRTEM analysis of irregularly shaped NPs with [0 1 0] atomic resolution, FFT analysis is inserted, and the identified crystalline planes (*hkl*) corresponded to ZnO. c) ZnO-NPs 400 °C with quasi-spherical shapes (red circles). d) The HRTEM analysis with [0 1 0] atomic resolution, FFT analysis, and calculated interplanar distances for ZnO (PDF #891397).

(Kołodziejczak-Radzimska and Jesionowski, 2014). It has anti-inflammatory and wound healing properties, especially in its nanometric size (Król et al., 2017; Limo et al., 2018). Due to their high antimicrobial properties (Abebe et al., 2020; Kumar et al., 2017; Mishra et al, 2017), ZnO-NPs are found in personal care products (Oprea et al., 2014), incorporated into new food packaging alternatives (Motelica et al., 2020, 2021), or used for medical purposes (Fasiku et al., 2020; Martínez-Carmona et al., 2018).

One of the methods used to synthesize ZnO-NPs is green synthesis, where plant extracts are used as a reducing medium (Chan et al., 2021). In this work, the extract of *Dysphania ambrosiodes* was used, which is consumed in Mexican traditional medicine as infusions or decoctions of the leaves and roots, as well as its essential oil for its use as an anthelmintic, antiparasitic, etc. Monoterpenes and sesquiterpenes have been identified among their components, mainly ascaridol and limonene, *trans*-pinocarveol, aritasone, β-pinene, myrcene, camphor, and α-terpineol in addition to phenolic compounds such as flavones and flavonols, most of them quercetin and kaempferol derivatives (Carrillo-López et al., 2016; Gómez-Castellanos, 2008).

The ZnO-NPs green synthesis mechanism using *Dysphania ambrosiodes* extract (Fig. 8) has been associated with polyphenols and terpenes interactions as binding agents. Zinc ions ($Zn^{2+}$) make coordination compounds, and the fundamental structural unit is the central zinc ion surrounded by four coordinate groups spatially arranged at the corners of a regular tetrahedron. Polyphenol aromatic hydroxyl (–OH) groups bind to $Zn^{2+}$ and form a stable coordination complex. This system undergoes direct decomposition above 200 °C, leading to the release of NPs from the complex system (Nava et al., 2017).

Flavonoids, terpenes, tannins, reducing sugars, etc., have the characteristic of possessing –OH groups that surround $Zn^{2+}$ by losing electrons, forming the complex. After this process, the $OH^{1-}$ ions are oxidized to carbonyl groups. The carbonyl groups are involved in NPs stabilization. The synthesis is favored if the molecules involved have at least two –OH groups in ortho and para positions (Carrillo-López et al., 2016; Nava et al., 2017; Yuvakkumar et al., 2014).

The concentration and type of amino acids present in the extract, combined with the reaction conditions, give rise to a wide variety of NPs (Limo et al., 2018; Makarov et al.,

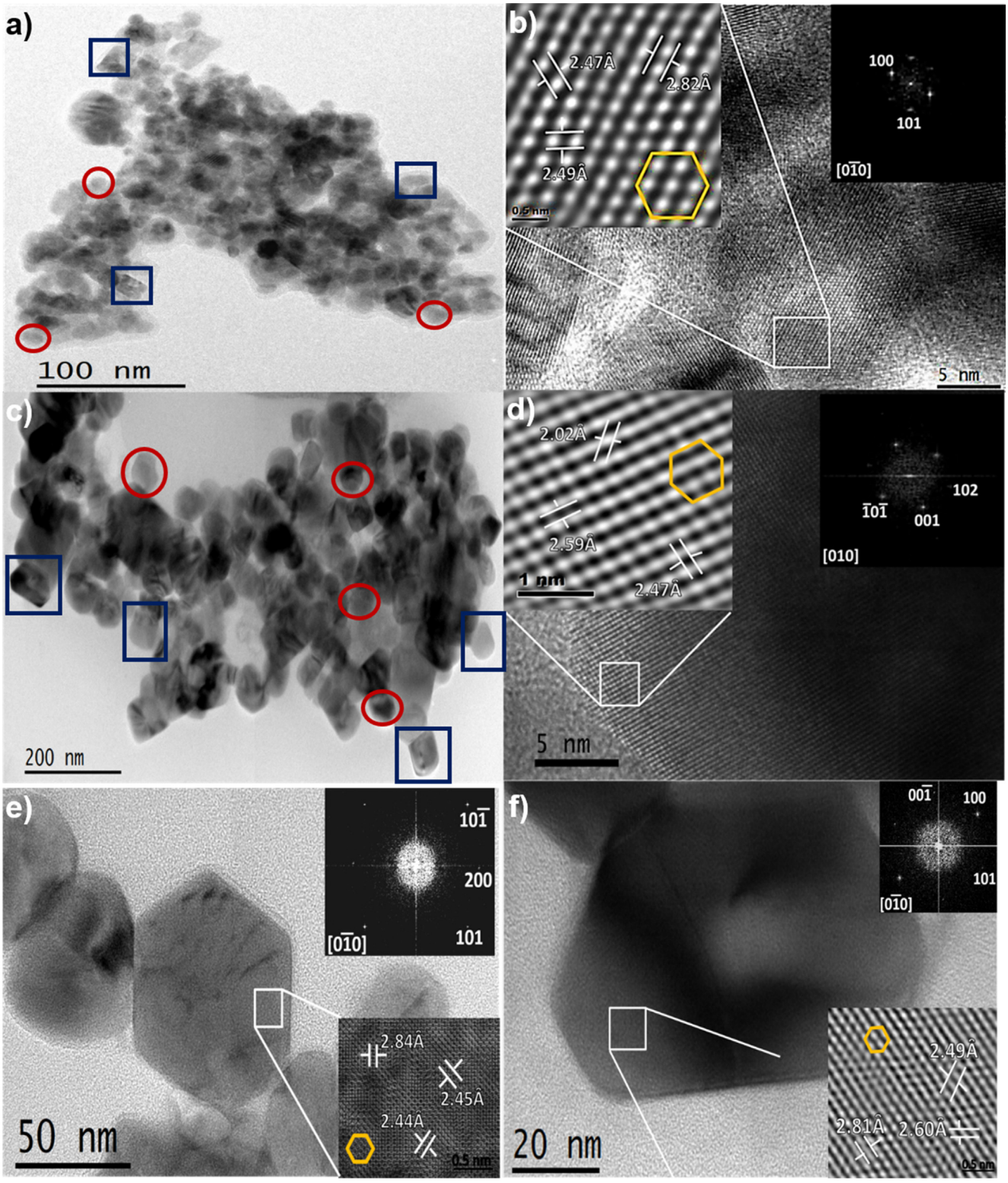


**Fig. 5** TEM images of ZnO-NPs 600 °C and ZnO-NPs 800 °C. a) ZnO-NPs 600 °C with quasi-spherical shapes (red circles) and hexagonal prism shapes (blue squares). b) The HRTEM analysis of the quasi-spherical shaped ZnO-NPs 600 °C with atomic resolution in the [0 1 0] direction, FFT analysis is inserted. c) ZnO-NPs 800 °C with quasi-spherical (red circles) and the hexagonal prism shapes (blue squares). d) The HRTEM images of the quasi-spherical shaped ZnO-NPs 800 °C with atomic resolution in the [0 1 0] direction. In FFT analysis, the ZnO interplanar distances (*hkl*) were identified. e) In the FTT analysis of the hexagonal prism-shaped ZnO-NPs 600 °C in the [0 1 0] direction, ZnO interplanar distances are indicated. f) In the FTT analysis of the hexagonal prism-shaped ZnO-NPs 800 °C in [0 1 0] direction, ZnO interplanar distances are indicated.

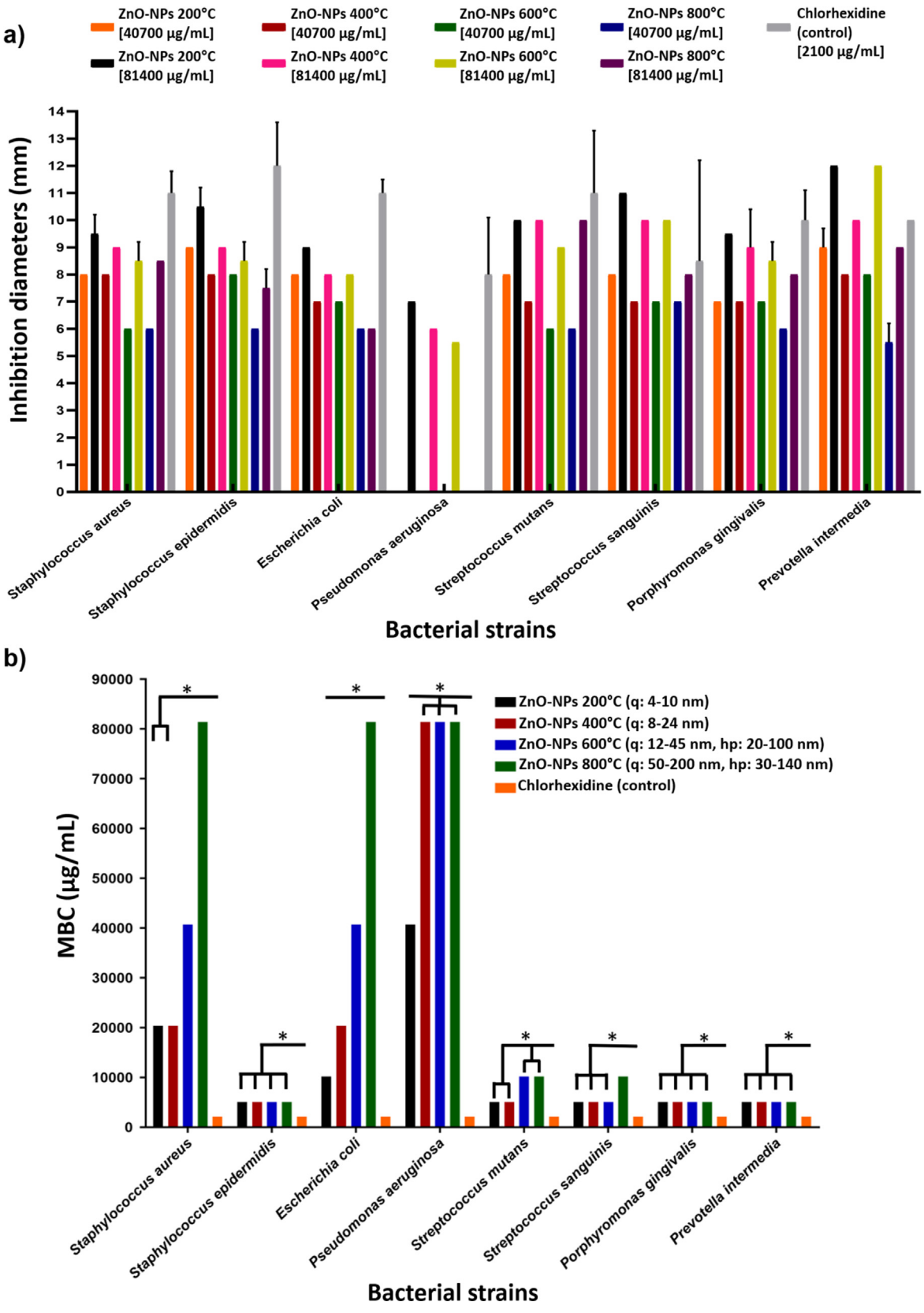


**Fig. 6** a) Mean measurements and standard deviation bars in mm of the inhibition diameters generated by ZnO-NPs. The 6 mm disk diameter is included. b) The MBC in µg/mL of the ZnO-NPs of different particle sizes. q (quasi-spherical), hp (hexagonal prisms). Significance $P \leq 0.001$(*).

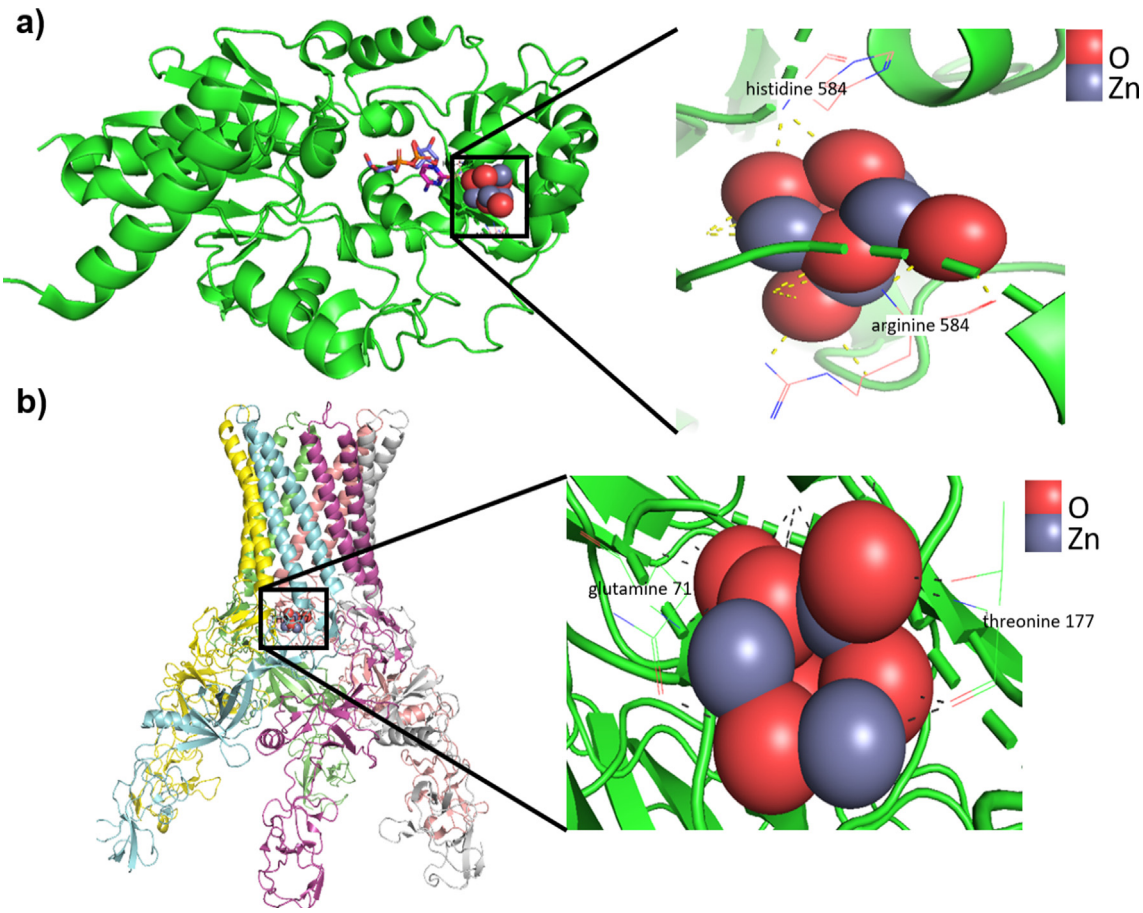


**Fig. 7** a) The binding mode simulation of ZnO-NPs to the *Staphylococcus epidermidis* TagF protein shows the probable binding site and the hydrogen bonds between ZnO-NPs and arginine 548 and histidine 584 amino acids in this protein. b) The binding mode simulation of ZnO-NPs to the *Escherichia coli* AcrAB-TolC pump shows the probable binding site and the hydrogen bonds between ZnO-NPs and glutamine 71 and threonine 177 amino acids.

2014), as seen in this study, where mostly quasi-spherical and hexagonal prism shapes were synthesized.

The ZnO hexagonal crystalline structure was confirmed by XRD analysis. The positions of indexed reflections coincided with the diffraction patterns of synthesized ZnO-NPs at different temperatures and with the standard diffraction pattern for ZnO indicated in PDF #891397, used as a reference. The intensities were different, which is related to crystalline size. The average crystalline size was calculated with the Debye-Scherrer equation, and it was found that the average crystalline size increased as the temperature was higher. These results supported HRTEM image analysis where ZnO crystalline planes in all synthesized ZnO-NPs were determined.

As was mentioned in the results section, the FESEM and TEM images showed the different sizes and shapes of the synthesized ZnO-NPs. The difference between the crystallite size and the nanoparticle size indicates they are polycrystalline.

These results coincide with green synthesized ZnO-NPs using other vegetal species. For example, with *Pandanus odorifer*, spherical NPs of 90 nm at 400 and 600 °C were synthesized (Hussain et al., 2019). With *Medicago sativa*, quasi-spherical NPs of 10 nm at 110 °C were synthesized (Król et al., 2019). Spherical-shaped NPs ranging from 25 to 90 nm were synthesized with *Trianthema portulacastrum* (Khan et al., 2019). Using *Solanum torvum*, NPs ranging from 30 to 40 nm in spherical shape were synthesized at 60 °C (Ezealisiji et al., 2019). With *Trifolium pratense*, quasi-spherical NPs ranging from 100 to 190 nm at 400 °C were synthesized (Dobrucka et al., 2016). With *Brassica oleracea*, NPs ranging from 14 to 17 nm at 450 °C were synthesized (Osuntokun et al., 2019). NPs ranging from 20 to 40 nm were synthesized with *Berberis aristata* (Chandra et al., 2019). At 80 °C, with *Limonia acidissima*, NPs ranging from 12 to 45 nm in spherical shape were synthesized. (Patil and Taranath, 2016). NPs ranging from 9 to 18 nm in hexagonal prism shapes were synthesized with *Aloe vera* and *Hibiscus sabdariffa* (Mahendiran et al., 2017), which are very similar to those obtained in this study. NPs of 32.98 nm and 81.84 nm were synthesized with *Punica granatum* at 600 and 700 °C, respectively. Their shapes were quasi-spherical and hexagonal (Sukri et al., 2019). This result coincides with those obtained in this work. By increasing the synthesis temperature, the size of the NPs increased, and new shapes emerged. This result coincides with those obtained in this work; by increasing the synthesis temperature, the size of the NPs increased, and new shapes emerged.

Therefore, the plant species and the synthesis temperature influence the size and shape of the resulting NPs.

The growth of the hexagonal prism-shaped structure and quasi-spherical shaped structures of the ZnO-NPs is due to

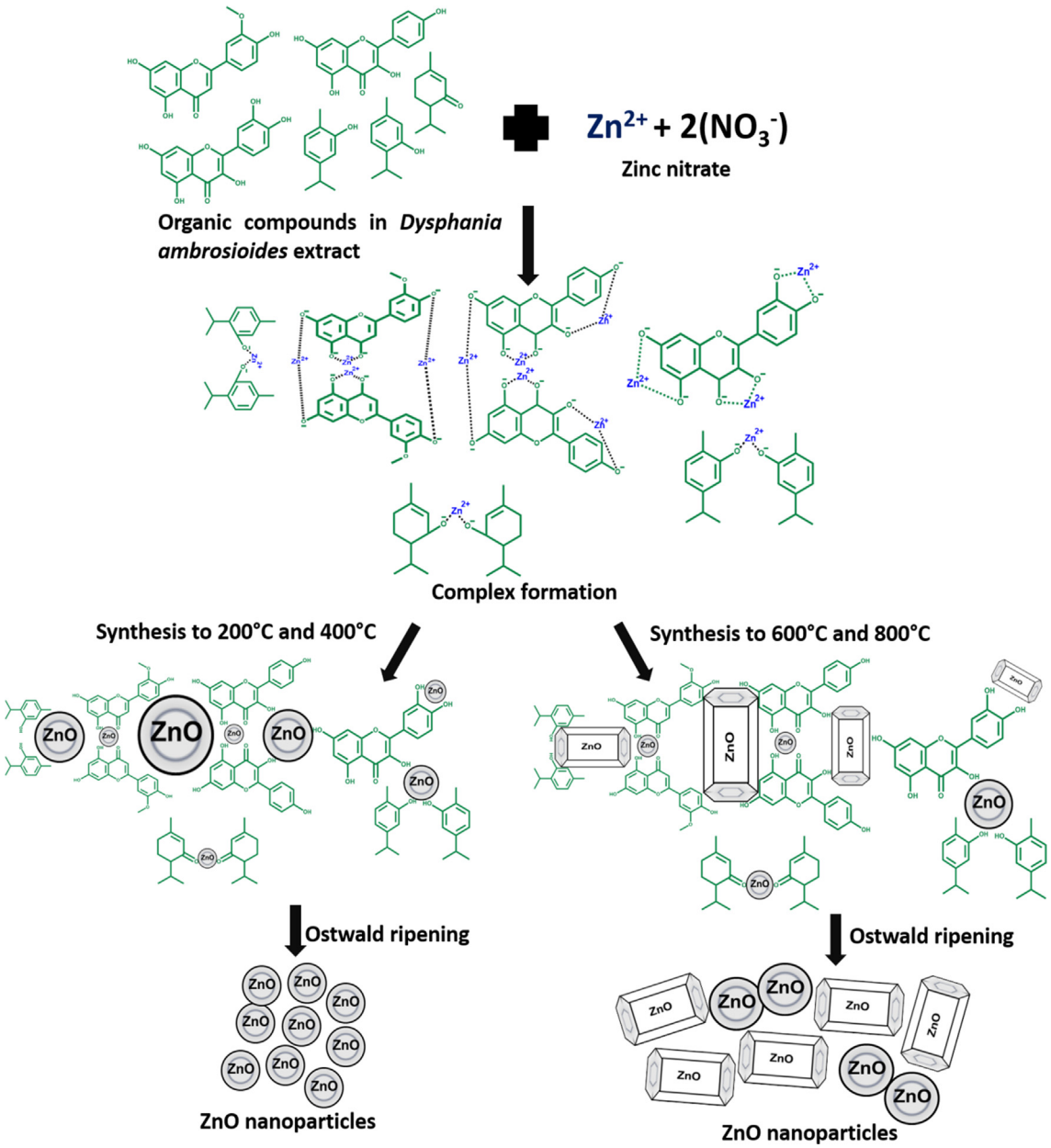


**Fig. 8** A proposed mechanism for the green synthesis of ZnO-NPs using *Dysphania ambrosioides* extract.

the presence of zincate ions $(Zn(OH)_4)^{2-}$ from the interaction of $Zn^{2+}$ with the $OH^{1-}$ ions in the plant extract. When the solution containing zincate ions is heated, it slowly converts into ZnO. This phenomenon occurs because the ZnO crystal structure is constructed gradually by $OH^{1-}$ ions, and acts as a polar crystal. When the particles become saturated, the ZnO nucleus grows, resulting in spherical or quasi-spherical-shaped nanoparticles. The heat treatment provides sufficient heat energy for atom nucleation and enhanced surface mobility allowing these structures to be placed onto the surface of previously formed hexagonal crystallites, which leads to the formation of the hexagonal prism-shaped structure. The organic compounds participate in the nucleation centers, stabilizing them, also influencing the resulting shapes, and defining the nanometric size. (Hassan et al., 2020; Kumar and Rani, 2013).

The EDS results analysis supported the confirmation of ZnO synthesis as the atomic percentages of Zn and O were close to 50%. A tendency was observed that, at higher synthesis temperatures, the atomic percentage of Zn increased and that of O decreased. This is because, at high temperatures, several organic compounds are degraded. These compounds have O in their structure, so when they are degraded, they no longer participate in the reaction as they cannot form the complex with Zn, which will form complexes with the remaining organic molecules (Krężel and Maret, 2014). The increase in temperature causes the release of surface oxygen, which also causes a decrease in its atomic percentage (Wang et al., 2018).

The ZnO increases its particle size by increasing the annealing temperature (Oprea et al., 2013). The influence of temperature on particle size in liquid-phase synthesis may be

explained by the phenomenon known as "Ostwald ripening," in which smaller particles are redissolved due to their high solubility and surface energy within the solution. At higher temperatures, there are more collisions of these redissolved particles, allowing the larger particles to grow further and reprecipitate into larger particles (Gommes, 2019; Thanh et al., 2014). This behavior was confirmed by analyzing the size of the synthesized ZnO-NPs at different temperatures, and it was observed that the particle size increased with higher temperatures.

The FTIR characterization of the synthesized ZnO-NPs at different temperatures showed the vibration corresponding to the Zn-O bond in all syntheses and the presence of other vibrations corresponding to the functional groups of the remaining organic compounds involved in the reaction (Anvekar et al., 2017; Khan et al., 2015; Liu et al., 2019; Santhoshkumar et al., 2017; Umar et al., 2018).

In TG analysis, the weight around 100 °C in all ZnO-NPs corresponded to water evaporation. At 150 °C, the weight loss in the ZnO-NPs 200 °C was caused by the decomposition of $Zn(OH)_2$, which was formed by diluting the $Zn(NO_3)_2$ in the extract and remained to be converted to ZnO, because it decomposes at temperatures above 125 °C (Wang et al., 2011). At 400 °C, the weight loss from the decomposition of nitrate groups and the remaining organic matter was 11.30% (Fatimah et al., 2016; Pinjari et al., 2016). At 550 °C, weight loss of 9.41% in the ZnO-NPs 400 °C, 11.61% in the ZnO-NPs 600 °C, and 9.41% in the ZnO-NPs 800 °C were caused by the decomposition of $NO_3^{1-}$ and $OH^{1-}$ groups, as well as the O evaporation (He et al., 2019; Pinjari et al., 2016). At 250 °C, the organic compound decomposition causes a weight loss of 1.01% in the ZnO-NPs 800 °C (Fatimah et al., 2016). The increase in synthesis temperature promotes higher stability of the ZnO-NPs due to the presence of oxygen vacancies in the ZnO crystalline structure. As the synthesis temperature increases, a greater number of oxygen vacancies appear, reaching a maximum when the synthesis is carried out at 600 °C, which is the temperature at which the greatest number of oxygen vacancies are generated. When the synthesis is above 600 °C, the ZnO-NPs begin to present a lower number of oxygen vacancies, which makes them more sensitive to the increase in temperature (He et al., 2019). This is why the ZnO-NPs 800 °C show a higher weight loss than the ZnO-NPs 600 °C.

The antibacterial tests showed that all the bacterial strains evaluated were sensitive to ZnO-NPs, and particle size did influence their inhibition or elimination.

Gram-positive and Gram-negative bacteria are structurally different; the cell wall of Gram-positive bacteria is a peptidoglycan layer of 20 to 50 nm bound to teichoic acids that are unique to these bacteria. In contrast, Gram-negative bacteria are more complex; the cell wall consists of a thin layer of peptidoglycan located in the middle of two membranes, the outer and inner membrane. The outer membrane contains lipopolysaccharides and proteins called porins, where the transport of nutrients and ions that are essential for the structural integrity and viability of the bacteria takes place (Hajipour et al., 2012). These structural differences influence Gram-positive bacteria to be generally more sensitive to NPs than Gram-negative bacteria because they do not have many protective barriers.

*Staphylococcus aureus* and *Staphylococcus epidermidis* were sensitive to ZnO-NPs, *Staphylococcus epidermidis* being one of the most sensitive. These results coincide with the inhibition achieved by ZnO-NPs of 50 nm evaluated at the same concentrations on these bacterial strains (Tayel et al., 2011). Gram-positive bacteria are usually the most sensitive to ZnO-NPs where inhibition diameters of 17–23 mm have been reported with NPs ranging from 10 to 90 nm, spherical and elongated shapes, and the MBC is also lower (Gaddala et al., 2014; Stan et al., 2016), conserving the characteristic that the smaller the size, the greater the inhibition and being concentration-dependent (Elumalai and Velmurugan, 2015).

*Escherichia coli* and *Pseudomonas aeruginosa* were also sensitive to ZnO-NPs, observing that NPs ranging from 14 to 25 nm and quasi-spherical shape inhibit them (Azam et al., 2012). The MBC is higher than with other Gram-positive bacteria and is also size-dependent (Iqbal et al., 2019; Mirza et al., 2019). *Pseudomonas aeruginosa* was the most resistant to NPs (Elumalai and Velmurugan, 2015), coinciding with the results obtained in this work.

The growth inhibition of *Streptococcus mutans, Streptococcus sanguinis*, *Prevotella intermedia,* and *Porphyromonas gingivalis,* which are related to dental diseases, showed that these bacterial strains were the most sensitive to the ZnO-NPs. Larger inhibition diameters were generated and the MBCs were obtained at the lowest concentrations. It was observed that there was an influence of the particle size on their inhibition. The larger the NPs, the smaller the inhibition diameters. As for the MBC, only with *Streptococcus mutans* and *Streptococcus sanguinis* was it possible to observe an influence of particle size. The growth inhibition of *Streptococcus mutans, Streptococcus sanguinis, Prevotella intermedia,* and *Porphyromonas gingivalis* was similar to that obtained by ZnO-NPs, ranging from 10 to 50 nm, and irregular shape, generating inhibition diameters ranging from 12 to 17 mm (Vargas-Reus et al., 2012; Wang et al., 2019). The MBC results obtained in this work were higher than those reported in other investigations where bacteria inoculum destruction can occur at concentrations ranging from 0.3 μg/mL with 30 nm NPs (Modaresi, 2017) up to 2500 μg/mL with NPs ranging from 10 to 50 nm (Khan et al., 2016) or even enhance their inhibitory effect by placing them in mouthwashes where ZnO-NPs of 20 nm at a concentration of 25 μg/mL were able to inhibit them (Eslami et al., 2015).

These bacteria are involved in several dental diseases, such as dental caries, where *Streptococcus mutans* is the most commonly associated pathogen (Zhang, 2014). *Streptococcus sanguinis,* together with other bacteria, forms the yellow complex, one of the bases of the pyramid of Socransky that groups the different bacteria involved in periodontal disease development. The yellow complex participates in the initial colonization of the tooth surface and increases its proliferation in the early stages of the disease. *Prevotella intermedia* belongs to the orange complex, located in the middle of the pyramid. This complex groups the most bacteria and interacts with the bacteria of the base complexes of the pyramid to further aggravate the damage. It also acts as a bridge to the late colonizers that make up the red complex, the tip of the pyramid, where *Porphyromonas gingivalis* is located together with two other bacteria that generate the pathology and inflammatory response (Socransky et al., 1998; Socransky and Haffajee, 2005). Therefore, the ZnO-NPs could be an alternative to treating these conditions in their different stages of development.

The ZnO-NPs antibacterial mechanisms that have been studied are alteration of protein and enzyme functions by direct interaction, ROS generation, cell membrane damage by electrostatic interaction, DNA damage, and $Zn^{2+}$ release, which together enhance this property (Raghunath and Perumal, 2017) (Fig. 9).

One of the main ZnO-NPs antibacterial mechanisms is through the alteration of protein and enzyme functions when ZnO-NPs interact directly with these molecules and leads to the loss of their function, as was demonstrated in molecular docking analysis. This damage is increased due to the reaction between -SH groups in proteins and $Zn^{2+}$ released by ZnO-NPs. $Zn^{2+}$ oxidize the amino acid chain, leading to protein denaturation and loss of enzyme activity, resulting in metabolic and growth function blockage (Aggarwal et al., 2009; Lynch et al., 2020).

As was mentioned before, the molecular docking study showed that ZnO-NPs could interact with bacterial proteins or enzymes, enhancing their antibacterial properties. Although the free binding energies of both proteins were similar, Ki indicates the inhibitor concentration required for half of the active sites to be occupied (Ferreira et al, 2015; Yuriev et al., 2015). In both cases, a low concentration of NPs is required to inhibit these sites and thus their function.

The TagF polymerase is involved in catalyzing the nucleophilic substitution to bind glycerol-phosphate units in teichoic acid synthesis in the cell wall of *Staphylococcus aureus* and *Staphylococcus epidermidis* (Weidenmaier and Peschel, 2008). Teichoic acid deficiency compromises virulence, biofilm formation, and even bacteria protection (Eiff et al., 1999; Lovering et al., 2010), resulting in higher antibacterial activity by NPs against these kinds of bacteria and the fact that NPs can interact with amino acids present in the enzyme catalytic site. The AcrAB-TolC efflux pump is a protein that crosses the inner and outer membranes of Gram-negative bacteria; this pump vectorially transports diverse compounds with little chemical similarity, conferring *Escherichia coli* resistance to a broad spectrum of antibiotics (Du et al., 2014). These transporters act synergistically with the outer membrane by expelling drugs or toxic compounds from the inner membrane and periplasm space to the external environment (Abdali et al., 2016). Inactivation of this protein completely abrogates the output of various compounds and leads to increased susceptibility to several antimicrobial agents such as NPs. The binding site of NPs was similar to that reported for potential organic inhibitors (Weidenmaier and Peschel, 2008).

Another important antibacterial mechanism is ROS generation. These species originate in the medium of the NPs as a change in their electronic properties. The smaller the particle size, the more interaction there is between donor and acceptor active sites of electrons, which generates a cascade of reactions and, consequently, the concentration of these species increases (Ali et al., 2018; Sivakumar et al., 2018). The ROS are superoxide anion ($\bullet O_2^-$), hydroxyl radical ($\bullet OH$), and hydrogen peroxide ($H_2O_2$). One of the ROS targets is the electron transport chain, which leads to ATP production decreasing by attacking enzymes involved in bacterial metabolism; they cause damage to other processes such as proteins, lipids, cell wall synthesis, etc. (Jiang et al., 2020). Another consequence is lipid peroxidation, which leads to deterioration of membrane integrity and conformational changes in membrane proteins. Finally, this imbalance between oxidants and antioxidants causes oxidative stress within the bacteria, leading to cell death (Dutta et al., 2012).

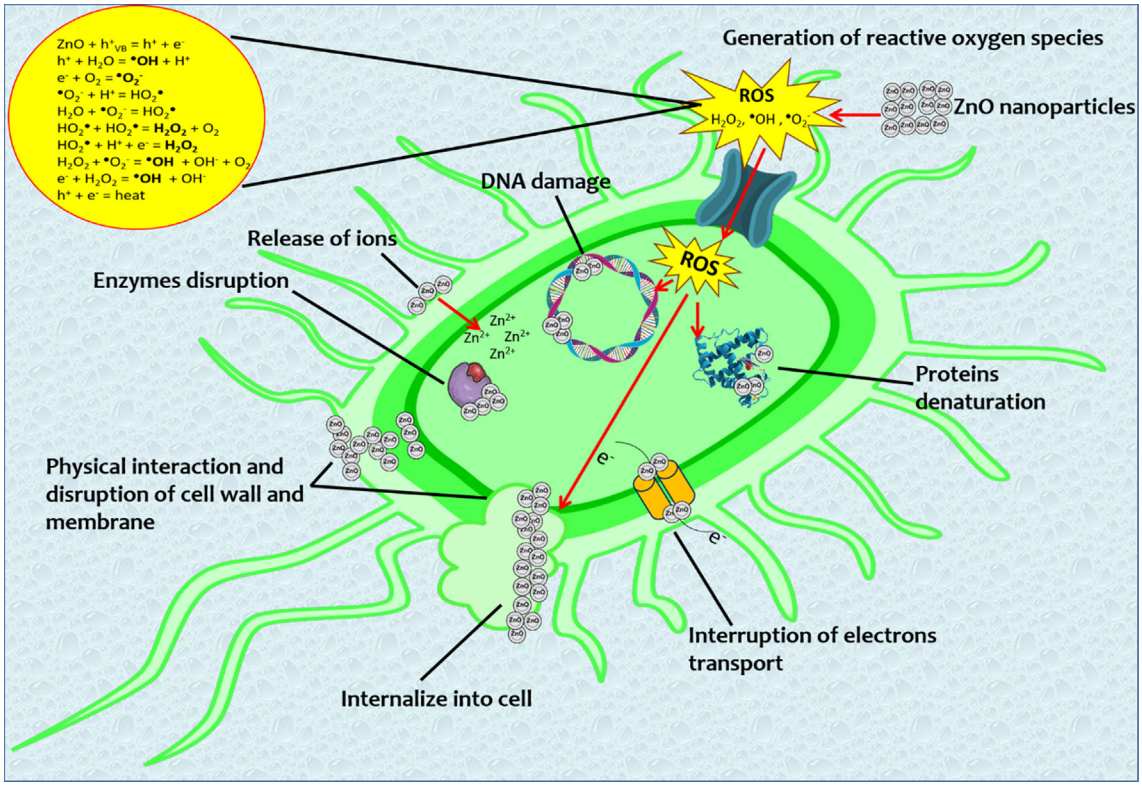


**Fig. 9** ZnO-NPs antibacterial mechanisms.

DNA damage is caused by a similar mechanism where ZnO-NPs intercalate into this structure or $Zn^{2+}$ react with the phosphate group of nucleotides (Nair et al., 2008).

The electrostatic interaction that leads to cell membrane damage is due to the charge differences between the negatively charged membrane and the generally positively charged ZnO-NPs, which causes them to accumulate in this structure. The NPs, depending on their size, will have a larger surface area, allowing higher interaction with the membrane, causing its alteration and subsequent permeability (Król et al., 2017). In addition, Gram-negative bacteria are susceptible to outer membrane damage because they contain lipopolysaccharides, which increase the negative charge compared to Gram-positive bacteria that do not have this structure (Beveridge, 1999).

Bacterial resistance mechanisms to different sized ZnO-NPs, mainly observed with *Pseudomonas aeruginosa*, are due to the production of extracellular matrix responsible for NPs agglomeration and deactivation, biofilm formation, electrical charge regulation of their surface or gene overexpression related to oxidative stress control, and active expulsion pumps, which allow the bacteria to reduce the generated damage (Niño-Martínez et al., 2019). These mechanisms are still under study, but as observed in this work, the antibacterial activity is different for each bacteria strain evaluated and where NPs particle size is an important property.

Nanometer-sized antibacterials have the potential to prevent the development of many diseases by controlling bacterial growth and biofilm formation (Allaker, 2011; Li et al., 2015). The ZnO-NPs, because of their antibacterial, anti-adhesive, and release properties, as well as their combinations with adhesives, polymers, resins, or surface coatings (Allaker, 2010; Allaker, 2011), broaden the range of possible antibacterial applications, including clinical use in the treatment of several bacterial-related diseases.

## 5. Conclusion

The green synthesis process using *Dysphania ambrosioides* extract allowed synthesizing ZnO-NPs of different sizes, on average ranging from 7 to 130 nm depending on the applied temperature (200, 400, 600, and 800 °C). The synthesis temperature influenced the obtained sizes and shapes of the ZnO-NPs. At higher temperatures, their sizes increased, and quasi-spherical and hexagonal prism shapes appeared. The synthesis of the ZnO-NPs, their sizes, shapes, stability, and ZnO crystalline structures were analyzed by characterization techniques. The influence of ZnO-NPs sizes on bacterial strain inhibition was demonstrated by higher inhibition or elimination of the strain with smaller ZnO-NPs (4–10 nm). This was mainly observed with *Staphylococcus aureus* and *Escherichia coli* strains, although all the evaluated strains were sensitive to ZnO-NPs. The molecular docking analysis evidenced the possible interaction between ZnO-NPs and bacterial proteins, as they are potential targets of ZnO-NPs, which would explain one of the bacterial inhibition mechanisms.

## Declaration of Competing Interest

The authors declare that they have no known competing financial interests or personal relationships that could have appeared to influence the work reported in this paper.

## Acknowledgment

To the Programa de Maestría y Doctorado en Ciencias Médicas, Odontológicas y de la Salud (PMDCMOS), Facultad de Odontolgía of the Universidad Nacional Autónoma de México (UNAM) and the Consejo Nacional de Ciencia y Tecnología (CONACYT) for the scholarship granted to R.A.C with CVU number: 579637, to R.T.H with CVU number: 662794, and to L.R.C with CVU number: 719797. The authors also thank Dr. Samuel Tehuacanero Cuapa, Mr. Antonio Morales Espino, Phys. Roberto Hernández Reyes, M.Sc. Manuel Aguilar Franco, M.Sc. Eréndira Martínez Acevedo, and Ar. Diego Quiterio Vargas for the technical support. Funds were provided by the "Programa de Apoyo a Proyectos de Investigación e Innovación Tecnológica (PAPIIT)" project IN112422.

## References

Abdali, N., Parks, J.M., Haynes, K.M., Chaney, J.L., Green, A.T., Wolloscheck, D., Walker, J.K., Rybenkov, V.V., Baudry, J., Smith, J.C., Zgurskaya, H.I., 2016. Reviving Antibiotics: Efflux Pump Inhibitors That Interact with AcrA, a Membrane Fusion Protein of the AcrAB-TolC Multidrug Efflux Pump. ACS Infect. Dis. 3 (1), 89–98. https://doi.org/10.1021/acsinfecdis.6b00167.

Abdelghany, A.M., Menazea, A.A., Abd-El-Maksoud, M.A., Khatab, T.K., 2019. Pulsed laser ablated zeolite nanoparticles: A novel nano-catalyst for the synthesis of 1,8-dioxo-octahydroxanthene and N -aryl-1,8-dioxodecahydroacridine with molecular docking validation. Appl. Organomet. Chem. 34. https://doi.org/10.1002/aoc.5250.

Abebe, B., Zereffa, E.A., Tadesse, A., Murthy, H.C.A., 2020. A Review on Enhancing the Antibacterial Activity of ZnO: Mechanisms and Microscopic Investigation. Nanoscale Res. Lett. 15 (1). https://doi.org/10.1186/s11671-020-03418-6.

Agarwal, H., Kumar, S.V., Rajeshkumar, S., 2017. A Review on Green Synthesis of Zinc Oxide Nanoparticles – An Eco-Friendly Approach. Resour.-Effic. Technol. 3 (4), 406–413. https://doi.org/10.1016/j.reffit.2017.03.002.

Aggarwal, P., Hall, J.B., Mcleland, C.B., Dobrovolskaia, M.A., Mcneil, S.E., 2009. Nanoparticle Interaction with Plasma Proteins as It Relates to Particle Biodistribution, Biocompatibility and Therapeutic Efficacy. Adv. Drug Deliv. Rev. 61 (6), 428–437. https://doi.org/10.1016/j.addr.2009.03.009.

Ahmed, M.K., El-Naggar, M.E., Aldalbahi, A., El-Newehy, M.H., Menazea, A.A., 2020a. Methylene blue degradation under visible light of metallic nanoparticles scattered into graphene oxide using laser ablation technique in aqueous solutions. J. Mol. Liq. 315,. https://doi.org/10.1016/j.molliq.2020.113794 113794.

Ahmed, M.K., Menazea, A.A., Mansour, S.F., Al-Wafi, R., 2020b. Differentiation between cellulose acetate and polyvinyl alcohol nanofibrous scaffolds containing magnetite nanoparticles/graphene oxide via pulsed laser ablation technique for tissue engineering applications. J. Mater. Res. Technol. 9, 11629–11640. https://doi.org/10.1016/j.jmrt.2020.08.041.

Ahmed, M.K., Moydeen, A.M., Ismail, A.M., El-Naggar, M.E., Menazea, A.A., El-Newehy, M.H., 2021. Wound dressing properties of functionalized environmentally biopolymer loaded with selenium nanoparticles. J. Mol. Struct. 1225,. https://doi.org/10.1016/j.molstruc.2020.129138 129138.

Ali, J., Irshad, R., Li, B., Tahir, K., Ahmad, A., Shakeel, M., Khan, N.U., Khan, Z.U.H., 2018. Synthesis and Characterization of Phytochemical Fabricated Zinc Oxide Nanoparticles with Enhanced Antibacterial and Catalytic Applications. J. Photochem.

Photobiol., B 183, 349–356. https://doi.org/10.1016/j.jphotobiol.2018.05.006.
Allaker, R.P., 2011. The Use of Antimicrobial Nanoparticles to Control Oral Infections. Nano-Antimicrobials 395–425. https://doi.org/10.1007/978-3-642-24428-5_14.
Allaker, R., 2010. The Use of Nanoparticles to Control Oral Biofilm Formation. J. Dent. Res. 89 (11), 1175–1186. https://doi.org/10.1177/0022034510377794.
Álvarez-Chimal, R., García-Pérez, V.I., Álvarez-Pérez, M.A., Arenas-Alatorre, J.Á., 2021. Green Synthesis of ZnO Nanoparticles Using a *Dysphania ambrosioides* Extract. Structural Characterization and Antibacterial Properties. Materials Sci. Eng. C 118,. https://doi.org/10.1016/j.msec.2020.111540 111540.
Anastas, P.T., Warner, J.C., 2014. Green Chemistry: Theory and Practice. Oxford University Press, Oxford.
Anvekar, T., Rajendra, V., Kadam, H., 2017. Green Synthesis of ZnO Nano Particles, Its Characterization and Application. Material Sci. Research India 14 (2), 153–157. https://doi.org/10.13005/msri/140211.
Azam, A., Ahmed, O., Khan, H., Memic, A., 2012. Antimicrobial Activity of Metal Oxide Nanoparticles against Gram-Positive and Gram-Negative Bacteria: a Comparative Study. Int. J. Nanomed. 6003. https://doi.org/10.2147/ijn.s35347.
Beveridge, T.J., 1999. Structures of Gram-Negative Cell Walls and Their Derived Membrane Vesicles. J. Bacteriol. 181 (16), 4725–4733. https://doi.org/10.1128/jb.181.16.4725-4733.1999.
Carrillo-López, L.M., Soto-Hernández, R.M., Zavaleta-Mancera, H. A., Vilchis-Néstor, A.R., 2016. Study of the Performance of the Organic Extracts Of *Chenopodium ambrosioides* for Ag Nanoparticle Synthesis. J. Nanomaterials 2016, 1–13. https://doi.org/10.1155/2016/4714162.
Carrillo-López, L.M., Zavaleta-Mancera, H.A., Vilchis-Nestor, A., Soto-Hernández, R.M., Arenas-Alatorre, J., Trejo-Téllez, L.I., Gómez-Merino, F., 2014. Biosynthesis of Silver Nanoparticles Using *Chenopodium ambrosioides*. J. Nanomaterials 2014, 1–9. https://doi.org/10.1155/2014/951746.
Carrouel, F., Viennot, S., Ottolenghi, L., Gaillard, C., Bourgeois, D., 2010. Nanoparticles as Anti-Microbial, Anti-Inflammatory, and Remineralizing Agents in Oral Care Cosmetics: A Review of the Current Situation. Nanomaterials 10 (1), 140. https://doi.org/10.3390/nano10010140.
Chan, Y.Y., Pang, Y.L., Lim, S., Chong, W.C., 2021. Facile Green Synthesis of ZnO Nanoparticles Using Natural-Based Materials: Properties, Mechanism, Surface Modification and Application. J. Environ. Chem. Eng. 9, (4). https://doi.org/10.1016/j.jece.2021.105417 105417.
Chandra, H., Patel, D., Kumari, P., Jangwan, J., Yadav, S., 2019. Phyto-Mediated Synthesis of Zinc Oxide Nanoparticles of *Berberis aristata*: Characterization, Antioxidant Activity and Antibacterial Activity with Special Reference to Urinary Tract Pathogens. Mater. Sci. Eng., C 102, 212–220. https://doi.org/10.1016/j.msec.2019.04.035.
Dobrucka, R., Długaszewska, J., 2016. Biosynthesis and Antibacterial Activity of ZnO Nanoparticles Using *Trifolium pratense* Flower Extract. Saudi J. Biological Sciences 23 (4), 517–523. https://doi.org/10.1016/j.sjbs.2015.05.016.
Du, D., Wang, Z., James, N.R., Voss, J.E., Klimont, E., Ohene-Agyei, T., Venter, H., Chiu, W., Luisi, B.F., 2014. Structure of the AcrAB–TolC Multidrug Efflux Pump. Nature 509 (7501), 512–515. https://doi.org/10.1038/nature13205.
Dutta, R., Nenavathu, B.P., Gangishetty, M.K., Reddy, A., 2012. Studies on Antibacterial Activity of ZnO Nanoparticles by ROS Induced Lipid Peroxidation. Colloids Surf., B 94, 143–150. https://doi.org/10.1016/j.colsurfb.2012.01.046.
Eiff, C.V., Heilmann, C., Peters, G., 1999. New Aspects in the Molecular Basis of Polymer-Associated Infections Due to *Staphylococci*. Eur. J. Clin. Microbiol. Infect. Dis. 18 (12), 843–846. https://doi.org/10.1007/s100960050417.
Elumalai, K., Velmurugan, S., 2015. Green Synthesis, Characterization and Antimicrobial Activities of Zinc Oxide Nanoparticles from the Leaf Extract of *Azadirachta indica* (L.). Appl. Surf. Sci. 345, 329–336. https://doi.org/10.1016/j.apsusc.2015.03.176.
Eslami, N., Rajabi, O., Ghazvini, K., Barati, S., Ahrari, F., 2015. The Antimicrobial Sensitivity of *Streptococcus mutans* and *Streptococcus sangius* to Colloidal Solutions of Different Nanoparticles Applied as Mouthwashes. Dental Research J. 12 (1), 44. https://doi.org/10.4103/1735-3327.150330.
Ezealisiji, K.M., Siwe-Noundou, X., Maduelosi, B., Nwachukwu, N., Krause, R.W.M., 2019. Green Synthesis of Zinc Oxide Nanoparticles Using *Solanum torvum* (L) Leaf Extract and Evaluation of the Toxicological Profile of the ZnO Nanoparticles-Hydrogel Composite in Wistar Albino Rats. International Nano Letters 9 (2), 99–107. https://doi.org/10.1007/s40089-018-0263-1.
Fasiku, V.O., Owonubi, S.J., Malima, N.M., Hassan, D., Revaprasadu, N., 2020. Metal Oxide Nanoparticles: A Welcome Development for Targeting Bacteria. Antibiotic Materials Healthcare 261–286. https://doi.org/10.1016/b978-0-12-820054-4.00015-x.
Fatimah, I., Pradita, R.Y., Nurfalinda, A., 2016. Plant Extract Mediated of ZnO Nanoparticles by Using Ethanol Extract of Mimosa Pudica Leaves and Coffee Powder. Procedia Eng. 148, 43–48. https://doi.org/10.1016/j.proeng.2016.06.483.
Ferreira, L., Santos, R.D., Oliva, G., Andricopulo, A., 2015. Molecular Docking and Structure-Based Drug Design Strategies. Molecules 20 (7), 13384–13421. https://doi.org/10.3390/molecules200713384.
Gaddala, B., Nataru, S., 2014. Biological Synthesis of Zinc Oxide Nanoparticles from *Catharanthus roseus* (l.) G. Don. Leaf Extract and Validation for Antibacterial Activity. International Journal of Drug Development & Research 6, 208–214.
Geetha, M., Nagabhushana, H., Shivananjaiah, H., 2016. Green Mediated Synthesis and Characterization of ZnO Nanoparticles Using *Euphorbia Jatropa* Latex as Reducing Agent. J. Sci.: Adv. Mater. Devices 1 (3), 301–310. https://doi.org/10.1016/j.jsamd.2016.06.015.
Ghanbari, D., Salavati-Niasari, M., Sabet, M., 2013. Preparation of flower-like magnesium hydroxide nanostructure and its influence on the thermal stability of poly vinyl acetate and Poly Vinyl Alcohol. Compos. B Eng. 45, 550–555. https://doi.org/10.1016/j.compositesb.2012.09.007.
Gómez-Castellanos, J.R., 2008. Epazote (*Chenopodium Ambrosioides*). Revisión a Sus Características Morfológicas, Actividad Farmacológica, y Biogénesis De Su Principal Principio Activo, Ascaridol. Boletín Latinoamericano y del Caribe de Plantas Medicinales y Aromáticas 7, 3–9.
Gommes, C.J., 2019. Ostwald Ripening of Confined Nanoparticles: Chemomechanical Coupling in Nanopores. Nanoscale 11 (15), 7386–7393. https://doi.org/10.1039/c9nr01349k.
Gunalan, S., Sivaraj, R., Rajendran, V., 2012. Green Synthesized ZnO Nanoparticles against Bacterial and Fungal Pathogens. Progress Natural Science: Materials International 22 (6), 693–700. https://doi.org/10.1016/j.pnsc.2012.11.015.
Hajipour, M.J., Fromm, K.M., Ashkarran, A.A., Aberasturi, D.J.D., Larramendi, I.R.D., Rojo, T., Serpooshan, V., Parak, W.J., Mahmoudi, M., 2012. Antibacterial Properties of Nanoparticles. Trends Biotechnol. 30 (10), 499–511. https://doi.org/10.1016/j.tibtech.2012.06.004.
He, H., Cao, J., Fei, X., Duan, N., 2019. High-temperature annealing of ZnO nanoparticles increases the dissolution magnitude and rate in water by altering o vacancy distribution. Environ. Int. 130,. https://doi.org/10.1016/j.envint.2019.104930 104930.
Hassan Basri, H., Talib, R.A., Sukor, R., Othman, S.H., Ariffin, H., 2020. Effect of synthesis temperature on the size of ZnO nanoparticles derived from pineapple peel extract and antibacterial activity of ZnO–starch nanocomposite films. Nanomaterials 10, 1061. https://doi.org/10.3390/nano10061061.

Hussain, A., Oves, M., Alajmi, M.F., Hussain, I., Amir, S., Ahmed, J., Rehman, M.T., El-Seedi, H.R., Ali, I., 2019. Biogenesis of ZnO Nanoparticles Using *Pandanus odorifer* Leaf Extract: Anticancer and Antimicrobial Activities. RSC Adv. 9 (27), 15357–15369. https://doi.org/10.1039/c9ra01659g.

Iqbal, J., Abbasi, B.A., Mahmood, T., Kanwal, S., Ahmad, R., Ashraf, M., 2019. Plant-Extract Mediated Green Approach for the Synthesis of ZnONPs: Characterization and Evaluation of Cytotoxic, Antimicrobial and Antioxidant Potentials. J. Mol. Struct. 1189, 315–327. https://doi.org/10.1016/j.molstruc.2019.04.060.

Ismail, A.M., Ezzat, H.A., Menazea, A.A., Ibrahim, M.A., 2021. Synthesis, molecular spectroscopic analyses, and Computational Investigation using DFT:B3LYP/LANL2DZ Calculations for PVC/pani/go composite. J. Electron. Mater. 50, 4741–4751. https://doi.org/10.1007/s11664-021-09009-0.

Jiang, S., Lin, K., Cai, M., 2020. ZnO Nanomaterials: Current Advancements in Antibacterial Mechanisms and Applications. Front. Chem. 8. https://doi.org/10.3389/fchem.2020.00580.

Khan, S. H., R, S., Pathak, B., Fulekar, M., 2015. Photocatalytic Degradation of Organophosphate Pesticides (Chlorpyrifos) Using Synthesized Zinc Oxide Nanoparticle by Membrane Filtration Reactor under UV Irradiation. Frontiers in Nanoscience and Nanotechnology 1 (1), 23–27. 10.15761/fnn.1000105

Khan, S.T., Al-Khedhairy, A.A., Musarrat, J., Ahamed, M., 2016. Application of Nanoparticles in Oral Hygiene. Biomaterials and Tissue. Engineering Bulletin 3 (1–4), 35–49. https://doi.org/10.33263/bteb314.035049.

Khan, Z.U.H., Sadiq, H.M., Shah, N.S., Khan, A.U., Muhammad, N., Hassan, S.U., Tahir, K., Safi, S.Z., Khan, F.U., Imran, M., Ahmad, N., Ullah, F., Ahmad, A., Sayed, M., Khalid, M.S., Qaisrani, S.A., Ali, M., Zakir, A., 2019. Greener Synthesis of Zinc Oxide Nanoparticles Using *Trianthema portulacastrum* Extract and Evaluation of Its Photocatalytic and Biological Applications. J. Photochem. Photobiol., B 192, 147–157. https://doi.org/10.1016/j.jphotobiol.2019.01.013.

Kołodziejczak-Radzimska, A., Jesionowski, T., 2014. Zinc Oxide—From Synthesis to Application: A Review. Materials 7 (4), 2833–2881. https://doi.org/10.3390/ma7042833.

Krężel, A., Maret, W., 2016. The Biological Inorganic Chemistry of Zinc Ions. Arch. Biochem. Biophys. 611, 3–19. https://doi.org/10.1016/j.abb.2016.04.010.

Król, A., Pomastowski, P., Rafińska, K., Railean-Plugaru, V., Buszewski, B., 2017. Zinc Oxide Nanoparticles: Synthesis, Antiseptic Activity and Toxicity Mechanism. Adv. Colloid Interface Sci. 249, 37–52. https://doi.org/10.1016/j.cis.2017.07.033.

Król, A., Railean-Plugaru, V., Pomastowski, P., Buszewski, B., 2019. Phytochemical Investigation of Medicago sativa L. Extract and Its Potential as a Safe Source for the Synthesis of ZnO Nanoparticles: The Proposed Mechanism of Formation and Antimicrobial Activity. Phytochem. Lett. 31, 170–180. https://doi.org/10.1016/j.phytol.2019.04.009.

Kumar, H., Rani, R., 2013. Structural and optical characterization of ZnO nanoparticles synthesized by microemulsion route. Int. Lett. Chem. Physics Astronomy 19, 26–36. https://doi.org/10.18052/www.scipress.com/ilcpa.19.26.

Kumar, R., Umar, A., Kumar, G., Nalwa, H.S., 2017. Antimicrobial Properties of ZnO Nanomaterials: A Review. Ceram. Int. 43 (5), 3940–3961. https://doi.org/10.1016/j.ceramint.2016.12.062.

Li, H., Chen, Q., Zhao, J., Urmila, K., 2015. Enhancing the Antimicrobial Activity of Natural Extraction Using the Synthetic Ultrasmall Metal Nanoparticles. Sci. Rep. 5 (1). https://doi.org/10.1038/srep11033.

Limo, M.J., Sola-Rabada, A., Boix, E., Thota, V., Westcott, Z.C., Puddu, V., Perry, C.C., 2018. Interactions between Metal Oxides and Biomolecules: from Fundamental Understanding to Applications. Chem. Rev. 118 (22), 11118–11193. https://doi.org/10.1021/acs.chemrev.7b00660.

Liu, Z., Chen, F., Lu, Z., 2019. Biofabrication of Zinc Oxide Nanoparticles, Characterization and Cytotoxicity against Pediatric Leukemia Cell Lines. Green Process. Synth, 9 (1), 56–62. https://doi.org/10.1515/gps-2020-0007.

Lovering, A.L., Lin, L.-Y.-C., Sewell, E.W., Spreter, T., Brown, E. D., Strynadka, N.C.J., 2010. Structure of the Bacterial Teichoic Acid Polymerase TagF Provides Insights into Membrane Association and Catalysis. Nat. Struct. Mol. Biol. 17 (5), 582–589. https://doi.org/10.1038/nsmb.1819.

Lynch, I., Dawson, K.A., 2020. Protein-Nanoparticle Interactions. Nano-Enabled Medical Applications 231–250. https://doi.org/10.1201/9780429399039-8.

Mahendiran, D., Subash, G., Selvan, D.A., Rehana, D., Kumar, R. S., Rahiman, A.K., 2017. Biosynthesis of Zinc Oxide Nanoparticles Using Plant Extracts of *Aloe vera* and *Hibiscus sabdariffa*: Phytochemical, Antibacterial Antioxidant and Anti-Proliferative Studies. BioNanoScience 7 (3), 530–545. https://doi.org/10.1007/s12668-017-0418-y.

Makarov, V.V., Love, A.J., Sinitsyna, O.V., Makarova, S.S., Yaminsky, I.V., Taliansky, M.E., Kalinina, N.O., 2014. "Green" Nanotechnologies: Synthesis of Metal Nanoparticles Using Plants. Acta Naturae 6 (1), 35–44. https://doi.org/10.32607/20758251-2014-6-1-35-44.

Martínez-Carmona, M., Gun'Ko, Y., Vallet-Regí, M., 2018. ZnO Nanostructures for Drug Delivery and Theranostic Applications. Nanomaterials 8 (4), 268. 10.3390/nano8040268

McConkey, B.J., Sobolev, V., Edelman, M., 2002. The Performance of Current Methods in Ligand-Protein Docking. Current Science Association 83 (7), 845–856.

Menazea, A.A., Ismail, A.M., Samy, A., 2021. Novel green synthesis of zinc oxide nanoparticles using orange waste and its thermal and antibacterial activity. J. Inorg. Organomet. Polym Mater. 31, 4250–4259. https://doi.org/10.1007/s10904-021-02074-2.

Meng, X.-Y., Zhang, H.-X., Mezei, M., Cui, M., 2011. Molecular Docking: A Powerful Approach for Structure-Based Drug Discovery. Current Computer Aided-Drug Design 7 (2), 146–157. https://doi.org/10.2174/157340911795677602.

Meraat, R., Ziabari, A.A., Issazadeh, K., Shadan, N., Jalali, K.M., 2016. Synthesis and Characterization of the Antibacterial Activity of Zinc Oxide Nanoparticles against *Salmonella Typhi*. Acta Metallurgica Sinica (English Letters) 29 (7), 601–608. https://doi.org/10.1007/s40195-016-0439-5.

Mirza, A.U., Kareem, A., Nami, S.A., Bhat, S.A., Mohammad, A., Nishat, N., 2019. *Malus pumila* and *Juglen regia* Plant Species Mediated Zinc Oxide Nanoparticles: Synthesis, Spectral Characterization, Antioxidant and Antibacterial Studies. Microb. Pathog. 129, 233–241. https://doi.org/10.1016/j.micpath.2019.02.020.

Mishra, P.K., Mishra, H., Ekielski, A., Talegaonkar, S., Vaidya, B., 2017. Zinc Oxide Nanoparticles: a Promising Nanomaterial for Biomedical Applications. Drug Discovery Today 22 (12), 1825–1834. https://doi.org/10.1016/j.drudis.2017.08.006.

Modaresi, F., 2017. The Use of Synergistically Antiplaque Nanoparticles In Treating Dental Caries. Journal of Dental Health, Oral Disorders & Therapy 6 (5). 10.15406/jdhodt.2017.06.00214.

Mortazavi-Derazkola, S., Zinatloo-Ajabshir, S., Salavati-Niasari, M., 2015. Novel simple solvent-less preparation, characterization and degradation of the cationic dye over holmium oxide ceramic nanostructures. Ceram. Int. 41, 9593–9601. https://doi.org/10.1016/j.ceramint.2015.04.021.

Mostafa, A.M., Menazea, A.A., 2020. Laser-assisted for preparation ZnO/CDO thin film prepared by pulsed laser deposition for catalytic degradation. Radiat. Phys. Chem. 176,. https://doi.org/10.1016/j.radphyschem.2020.109020 109020.

Motelica, L., Ficai, D., Ficai, A., Truşcă, R.-D., Ilie, C.-I., Oprea, O.-C., Andronescu, E., 2020. Innovative antimicrobial chitosan/ZnO/AgNPS/citronella essential oil nanocomposite—potential coating for grapes. Foods 9, 1801. https://doi.org/10.3390/foods9121801.

Motelica, L., Ficai, D., Oprea, O., Ficai, A., Trusca, R.-D., Andronescu, E., Holban, A.M., 2021. Biodegradable alginate films with ZnO nanoparticles and Citronella Essential Oil—a novel antimicrobial structure. Pharmaceutics 13, 1020. https://doi.org/10.3390/pharmaceutics13071020.

Nair, S., Sasidharan, A., Rani, V.V.D., Menon, D., Nair, S., Manzoor, K., Raina, S., 2008. Role of Size Scale of ZnO Nanoparticles and Microparticles on Toxicity toward Bacteria and Osteoblast Cancer Cells. J. Mater. Sci. - Mater. Med. 20 (S1), 235–241. https://doi.org/10.1007/s10856-008-3548-5.

Nava, O., Luque, P., Gómez-Gutiérrez, C., Vilchis-Nestor, A., Castro-Beltrán, A., Mota-González, M., Olivas, A., 2017. Influence of *Camellia sinensis* Extract on Zinc Oxide Nanoparticle Green Synthesis. J. Mol. Struct. 1134, 121–125. https://doi.org/10.1016/j.molstruc.2016.12.069.

Niño-Martínez, N., Orozco, M.F.S., Martínez-Castañón, G.-A., Méndez, F.T., Ruiz, F., 2019. Molecular Mechanisms of Bacterial Resistance to Metal and Metal Oxide Nanoparticles. Int. J. Mol. Sci. 20 (11), 2808. https://doi.org/10.3390/ijms20112808.

Oprea, O., Vasile, O.R., Voicu, G., Andronescu, E., 2013. The influence of the thermal treatment on luminescence properties of ZnO. Digest J. Nanomaterials Biostructures 8 (2), 747–756.

Oprea, O., Andronescu, E., Ficai, D., Ficai, A., Oktar, F., Yetmez, M., 2014. ZnO applications and challenges. Curr. Org. Chem. 18, 192–203. https://doi.org/10.2174/1385272813176660143.

Osuntokun, J., Onwudiwe, D.C., Ebenso, E.E., 2019. Green Synthesis of ZnO Nanoparticles Using Aqueous *Brassica oleracea* L. Var. Italica and the Photocatalytic Activity. Green Chem. Lett. Rev. 12 (4), 444–457. https://doi.org/10.1080/17518253.2019.1687761.

Özgür, Ü., Alivov, Y.I., Liu, C., Teke, A., Reshchikov, M.A., Doğan, S., Avrutin, V., Cho, S.-J., Morkoç, H., 2005. A Comprehensive Review of ZnO Materials and Devices. J. Appl. Phys. 98, (4). https://doi.org/10.1063/1.1992666 041301.

Patil, B.N., Taranath, T.C., 2016. *Limonia acidissima* L. Leaf Mediated Synthesis of Zinc Oxide Nanoparticles: A Potent Tool against *Mycobacterium tuberculosis*. Int. J. Mycobacteriology 5 (2), 197–204. https://doi.org/10.1016/j.ijmyco.2016.03.004.

Pinjari, D., Pandit, A.B., Mhaske, S., 2016. Ultrasound Assisted Green Synthesis of Zinc Oxide Nanorods at Room Temperature. Indian J. Chem. Technol. 23 (3), 221–226.

Raghunath, A., Perumal, E., 2017. Metal Oxide Nanoparticles as Antimicrobial Agents: a Promise for the Future. Int. J. Antimicrob. Agents 49 (2), 137–152. https://doi.org/10.1016/j.ijantimicag.2016.11.011.

Salavati-Niasari, M., 2004. Zeolite-encapsulation copper(ii) complexes with 14-membered hexaaza macrocycles: Synthesis, characterization and catalytic activity. J. Mol. Catal. A: Chem. 217, 87–92. https://doi.org/10.1016/j.molcata.2004.02.022.

Salavati-Niasari, M., Hasanalian, J., Najafian, H., 2004. Alumina-supported $FeCl_3$, $MnCl_2$, $CoCl_2$, $NiCl_2$, $CuCl_2$, and $ZnCl_2$ as catalysts for the benzylation of benzene by benzyl chloride. J. Mol. Catal. A: Chem. 209, 209–214. https://doi.org/10.1016/j.molcata.2003.08.027.

Salavati-Niasari, M., Davar, F., Mazaheri, M., 2008. Synthesis of $Mn_3O_4$ nanoparticles by thermal decomposition of a [bis(salicylidiminato)manganese(ii)] complex. Polyhedron 27, 3467–3471. https://doi.org/10.1016/j.poly.2008.04.015.

Salavati-Niasari, M., Ghanbari, D., Davar, F., 2009. Synthesis of different morphologies of bismuth sulfide nanostructures via hydrothermal process in the presence of thioglycolic acid. J. Alloy. Compd. 488, 442–447. https://doi.org/10.1016/j.jallcom.2009.08.152.

Salavati-Niasari, M., Sobhani, A., Davar, F., 2010a. Synthesis of star-shaped PBS nanocrystals using single-source precursor. J. Alloy. Compd. 507, 77–83. https://doi.org/10.1016/j.jallcom.2010.06.062.

Salavati-Niasari, M., Davar, F., Loghman-Estarki, M.R., 2010b. Controllable synthesis of thioglycolic acid capped ZnS(pn)0.5 nanotubes via simple aqueous solution route at low temperatures and conversion to wurtzite ZnS nanorods via thermal decompose of precursor. J. Alloy. Compd. 494, 199–204. https://doi.org/10.1016/j.jallcom.2009.10.265.

Salinas Estevané, J.P., Sánchez Cervantes, E.M., 2012. La Química Verde En La Síntesis De Nanoestructuras. Ingenierías 15, 7–16.

Santhoshkumar, J., Kumar, S.V., Rajeshkumar, S., 2017. Synthesis of Zinc Oxide Nanoparticles Using Plant Leaf Extract against Urinary Tract Infection Pathogen. Resour.-Effic. Technol. 3 (4), 459–465. https://doi.org/10.1016/j.reffit.2017.05.001.

Sirelkhatim, A., Mahmud, S., Seeni, A., Kaus, N.H.M., Ann, L.C., Bakhori, S.K.M., Hasan, H., Mohamad, D., 2015. Review on Zinc Oxide Nanoparticles: Antibacterial Activity and Toxicity Mechanism. Nano-Micro Letters 7 (3), 219–242. https://doi.org/10.1007/s40820-015-0040-x.

Sivakumar, P., Lee, M., Kim, Y.-S., Shim, M.S., 2018. Photo-Triggered Antibacterial and Anticancer Activities of Zinc Oxide Nanoparticles. J. Mater. Chem. B 6 (30), 4852–4871. https://doi.org/10.1039/c8tb00948a.

Socransky, S. S., Haffajee, A. D., 2005. Periodontal Microbial Ecology. Periodontology 2000 38 (1), 135–187. 10.1111/j.1600-0757.2005.00107.x

Socransky, S., Haffajee, A., Cugini, M., Smith, C., Kent, R.L., 1998. Microbial Complexes in Subgingival Plaque. J. Clin. Periodontol. 25 (2), 134–144. https://doi.org/10.1111/j.1600-051x.1998.tb02419.x.

Stan, M., Popa, A., Toloman, D., Silipas, T.D., Vodnar, D.C., 2016. Antibacterial and Antioxidant Activities of ZnO Nanoparticles Synthesized Using Extracts of *Allium sativum, Rosmarinus officinalis* and *Ocimum basilicum*. Acta Metallurgica Sinica (English Letters) 29 (3), 228–236. https://doi.org/10.1007/s40195-016-0380-7.

Sukri, S.N.A.M., Shameli, K., Wong, M.M.T., Teow, S.Y., Chew, J., Ismail, N.A., 2019. Cytotoxicity and Antibacterial Activities of Plant-Mediated Synthesized Zinc Oxide (ZnO) Nanoparticles Using *Punica granatum* (Pomegranate) Fruit Peels Extract. J. Mol. Struct. 1189, 57–65. https://doi.org/10.1016/j.molstruc.2019.04.026.

Tayel, A.A., El-Tras, W.F., Moussa, S., El-Baz, A.F., Mahrous, H., Salem, M.F., Brimer, L., 2011. Antibacterial Action Of Zinc Oxide Nanoparticles Against Foodborne Pathogens. J. Food Saf. 31 (2), 211–218. https://doi.org/10.1111/j.1745-4565.2010.00287.x.

Thanh, N.T.K., Maclean, N., Mahiddine, S., 2014. Mechanisms of Nucleation and Growth of Nanoparticles in Solution. Chem. Rev. 114 (15), 7610–7630. https://doi.org/10.1021/cr400544s.

Umar, H., Kavaz, D., Rizaner, N., 2018. Biosynthesis of Zinc Oxide Nanoparticles Using *Albizia Lebbeck* Stem Bark, and Evaluation of Its Antimicrobial, Antioxidant, and Cytotoxic Activities on Human Breast Cancer Cell Lines. Int. J. Nanomed. 14, 87–100. https://doi.org/10.2147/ijn.s186888.

Vargas-Reus, M.A., Memarzadeh, K., Huang, J., Ren, G.G., Allaker, R.P., 2012. Antimicrobial Activity of Nanoparticulate Metal Oxides against Peri-Implantitis Pathogens. Int. J. Antimicrob. Agents 40 (2), 135–139. https://doi.org/10.1016/j.ijantimicag.2012.04.012.

Vasile, B.S., Oprea, O., Voicu, G., Ficai, A., Andronescu, E., Teodorescu, A., Holban, A., 2014. Synthesis and characterization of a novel controlled release zinc oxide/gentamicin–chitosan composite with potential applications in wounds care. Int. J. Pharm. 463, 161–169. https://doi.org/10.1016/j.ijpharm.2013.11.035.

Wang, J., Chen, R., Xiang, L., Komarneni, S., 2018. Synthesis, properties and applications of ZnO nanomaterials with oxygen vacancies: A Review. Ceram. Int. 44, 7357–7377. https://doi.org/10.1016/j.ceramint.2018.02.013.

Wang, J., Du, L., Fu, Y., Jiang, P., Wang, X., 2019. ZnO Nanoparticles Inhibit the Activity of *Porphyromonas gingivalis* and *Actinomyces naeslundii* and Promote the Mineralization of the

Cementum. BMC Oral Health 19 (1). https://doi.org/10.1186/s12903-019-0780-y.

Wang, M., Zhou, Y., Zhang, Y., Hahn, S.H., Kim, E.J., 2011. From $Zn(OH)_2$ to ZnO: A study on the mechanism of phase transformation. CrystEngComm 13, 6024. https://doi.org/10.1039/c1ce05502j.

Webster, T.J., Seil, I., 2012. Antimicrobial Applications of Nanotechnology: Methods and Literature. Int. J. Nanomed. 2767. https://doi.org/10.2147/ijn.s24805.

Weidenmaier, C., Peschel, A., 2008. Teichoic Acids and Related Cell-Wall Glycopolymers in Gram-Positive Physiology and Host Interactions. Nat. Rev. Microbiol. 6 (4), 276–287. https://doi.org/10.1038/nrmicro1861.

Yuriev, E., Holien, J., Ramsland, P.A., 2015. Improvements, Trends, and New Ideas in Molecular Docking: 2012–2013 in Review. J. Mol. Recognit. 28 (10), 581–604. https://doi.org/10.1002/jmr.2471.

Yuvakkumar, R., Suresh, J., Nathanael, A.J., Sundrarajan, M., Hong, S., 2014. Novel Green Synthetic Strategy to Prepare ZnO Nanocrystals Using Rambutan (*Nephelium Lappaceum L.*) Peel Extract and Its Antibacterial Applications. Mater. Sci. Eng., C 41, 17–27. https://doi.org/10.1016/j.msec.2014.04.025.

Zhang, S., 2014. Dental Caries and Vaccination Strategy against the Major Cariogenic Pathogen. *Streptococcus mutans*. Current Pharmaceutical Biotechnology 14 (11), 960–966. https://doi.org/10.2174/1389201014666131226144339.